International Journal of Hydrogen Energy 73 (2024) 203–220

Contents lists available at ScienceDirect

International Journal of Hydrogen Energy

journal homepage: www.elsevier.com/locate/he

Innovative torque-based control strategy for hydrogen internal combustion engine

Pier Paolo Brancaleoni *, Enrico Corti, Vittorio Ravaglioli, Davide Moro, Giacomo Silvagni

DIN – Dipartimento di Ingegneria Industriale, Alma Mater Studiorum – Università di Bologna, Bologna, 40121, Italy

ARTICLE INFO

Keywords:
Hydrogen internal combustion engine
Artificial neural networks
H2ICE control strategy
H2ICE engine model
CA50 control

ABSTRACT

Over the past years, several efforts have been made to reduce greenhouse gas emissions coming from the transport sector. Due to the highly efficient CO2-free combustion and low manufacturing costs, Hydrogen Internal Combustion engines (H2ICEs) are considered one of the most promising solutions for the future of medium and heavy duty vehicles. However, the combustion of an air-hydrogen mixture presents challenges related to the production of nitrogen oxides (NOx) and high knock tendency, mainly due to the chemical characteristics of the fuel. Although these problems can be mitigated by the use of a lean mixture, which is also useful to increase the combustion efficiency, the presence of excess air reduces exhaust temperatures and, consequently, the enthalpy content in the exhaust would be limited, leading to a reduced boosting capability. Therefore, a proper control of mixture preparation and combustion phasing is mandatory to limit NOx emissions, avoid abnormal combustions, and maximize efficiency without performance limitations.

This paper focuses on the design of a dedicated control strategy for H2ICEs. Starting from a previously validated 1-D engine model operated with hydrogen, a 0-D Artificial Neural Network (ANN) - based engine model has been designed and calibrated. By using the obtained fast running ANN-based model, an innovative torque-based engine controller has been developed and both engine and controller models have been tested covering different torque profiles. The results show good accuracy within a range of ±5% on producing the requested torque by controlling the centre of combustion.

SYMBOLS/ABBREVIATIONS

ANN	Artificial Neural Network
BMEP	Brake Mean Effective Pressure
BSFC	Brake Specific Fuel Consumption
CA50	Crank Angle where 50% of fuel mass is burn
CCV	Cycle-to-Cycle Variability
CoV	Coefficient of Variation
EGR	Exhaust Gas Recirculation
EU	European Union
FCV	Fuel Cell Vehicle
FMEP	Friction Mean Effective Pressure
H2ICE	Hydrogen Internal Combustion Engine
H-DI	Hydrogen Direct Injection
H-PFI	Hydrogen Port Fuel Injection
IMEP	Indicated Mean Effective Pressure
IVC	Intake Valve Closing
λ	Relative air-to-fuel ratio
LuT	Look-up Table
MAP	Manifold Air Pressure
MAPO	Maximum Amplitude Pressure Oscillation
MAPO98	MAPO 98th Percentile
MBT	Maximum Brake Torque
MIL	Model in the Loop
NOx	Nitrogen Oxides
NSC	NOx Storage Catalyst
PFI	Port Fuel Injection
PI	Proportional Integral
PID	Proportional Integral Derivative
Pmax	Maximum in-cylinder Pressure
RMSE	Root Mean Squared Error
RMSE %	Root Mean Squared Error Percentage
RPM	Revolution per Minute
RON	Research Octane Number
SA	Spark Advance
SCR	Selective Catalyst Reduction
SI	Spark Ignited

(*continued on next column*)

(*continued*)

(*continued on next page*)

* Corresponding author.
E-mail addresses: pier.brancaleoni2@unibo.it (P.P. Brancaleoni), enrico.corti2@unibo.it (E. Corti), vittorio.ravaglioli2@unibo.it (V. Ravaglioli), davide.moro@unibo.it (D. Moro), giacomo.silvagni2@unibo.it (G. Silvagni).

https://doi.org/10.1016/j.ijhydene.2024.05.481
Received 19 February 2024; Received in revised form 30 April 2024; Accepted 31 May 2024
Available online 8 June 2024

(*continued*)

σ	Standard Deviation
TDC	Top Dead Centre
THR	Throttle valve
Tmax	Maximum in-cylinder Temperature
TtF	Torque to Fuel
VGT	Variable Geometry Turbine
ΔCA50	CA50 Degradation

1. Introduction

In recent years, the goal of reducing CO2 emissions of human activity has emerged as a priority on government and agency agendas [1]. The European Green Deal outlines the roadmap to address the challenge of climate change and achieve European Union (EU) climate neutrality by 2050 [2]. The 2022 gas and energy security crisis highlighted the importance of accelerating the transition toward clean and sustainable EU energy sources and technologies. As a result, several companies and researchers have been focused on investigating sustainable solutions to cut down greenhouse gases in key sectors of economy. In the EU, remarkable achievements in emissions reduction have been obtained over the past three decades, with the highest reductions occurring in the energy supply sector. However, the transport sector still struggles to cut down emissions. The use of renewable energy, low carbon fuels, synthetic fuels, ammonia, and hydrogen are considered the most promising solutions to accelerate this transition [3,4].

Because hydrogen combustion products are CO2-free, hydrogen-based propulsion technologies have emerged as one of the most promising solutions for the decarbonisation of the transport sector [5]. Among these, Fuel Cells (FCs) powertrains and Hydrogen Internal Combustion Engines (H2ICEs) represent the most studied technologies. Despite FCs being characterized by a higher energy conversion efficiency than H2ICEs [6], demanding standards on hydrogen quality and high manufacturing cost still are the main limitations for their widespread adoption [7].

Several works in literature tested conventional internal combustion engines operated with hydrogen and demonstrated easy integration with stock hardware [8–10]. Table 1 summarizes hydrogen, gasoline and diesel main chemical properties. Hydrogen shows a higher Lower Heating Value than gasoline and diesel. Despite having a higher Research Octane Number (RON), the minimum ignition energy promotes spontaneous localized ignitions. Moreover, with respect to conventional fuels, hydrogen can burn in a wider range of air-to-fuel ratio and with a much lower combustion duration due to its laminar flame speed. As regards emissions, conventional fuels are prone to Nitrogen Oxides (NOx) production due to high combustion temperature (above 1800 K) in slightly lean portion of the mixture combined with availability of oxygen [11]. Saravanan et al. [12] studied NOx formation in compression ignited diesel engines and discovered that flame temperature, molecular oxygen concentration, ignition delay and density of the fuel are the main factors influencing the rate of NOx formation. Luo et al. [13] studied NOx formation in turbocharged hydrogen fuelled engine, discovering that NOx formation is strictly related to engine speed, boost pressure (thus combustion temperature), spark timing and equivalence ratio, achieving peak NOx emissions of 7000 ppm. Heffel [14] studied the effect of Exhaust Gas Recirculation (EGR) on NOx formation in a 2.0 l multi cylinder engine, demonstrating that NOx emissions can be reduced down to 1 ppm. The adoption of lean combustion and EGR allows to drastically reduce NOx emissions, therefore, various combustion methodologies, including compression ignited, spark ignited, turbulent jet ignited, and several engine architectures were studied to enhance efficiency while minimizing NOx production [15–18]. These studies highlighted the advantages of hydrogen combustion in engine manufacturing, with high power-to-weight ratio, efficiency, and NOx emissions [10,19,20].

Table 1
Hydrogen and conventional fuels properties [21].

Property	Hydrogen	Gasoline	Diesel
Density (1 atm, 27 °C) [kg/m^3]	0.09	730–780	830
Flammability range in air [vol. %]	4–76	1–7.6	0.6–5.5
Auto-ignition temperature [K]	858	623	523
Laminar Flame Speed [m/s]	1.85	0.37–0.43	0.37–0.43
Minimum ignition energy [mJ]	0.02	0.24	0.24
Lower Heating Value [MJ/kg]	120	44.8	42.5
Stoichiometric air-to-fuel ratio [/]	34.5	14.7	14.5
Research Octane Number [/]	130	95	–

Despite H2ICEs share the entire engine platform with conventional ICEs, the injection systems are considered the most challenging components in hydrogen technology, especially in engine applications. Wang et al. [22] numerically investigated the effects of injection parameters on air-fuel mixture preparation in a 0.6 l spark-ignited engine equipped with Port Fuel hydrogen injection system (H-PFI). The authors demonstrated the influence of injection timings, nozzle hole positions, and nozzle hole area on the air-fuel mixture formation. They also highlighted the benefits of proper hydrogen-air mixing in terms of combustion performance and stability. However, despite being a cost effective solution, the injection of gaseous hydrogen in the intake stroke decreases the volumetric efficiency and might generate backfire (because the air-fuel mixture is within of the flammability range). According to Khalid et al. [23], for H-PFI the most crucial aspect on backfire is related to hot-spots in the combustion chamber and performing injection during the intake strokes allows to reduce the backfire risk.

Hydrogen Direct Injection (H-DI) is deeply investigated by Zhao et al. [22]. They both agreed that the introduction of gaseous hydrogen directly into the combustion chamber with proper timing (hydrogen injection must begin after Intake Valve Closing (IVC)) enhances the combustion efficiency and mitigates the risk of backfiring. Moreover, they also highlighted that spray targeting injection strategies promote the internal mixing processes with benefits on NOx and abnormal combustion events mitigation (i.e., knock, preignition, misfire).

Lai et al. [24] studied the inducing factors and characteristics of knock combustion testing a 2.0 l multi-cylinder spark ignited H-DI engine. The results revealed that equivalence ratio has greater impact on knock compared to injection phasing because of the extremely low activation energy of the mixture. As a result, several authors studied the effect of the mixture quality and combustion phasing and injection pressure on knock [24–27]. Lanz et al. [28,29] and Onorati et al. [28,29] documented that knocking combustion in H2ICEs is usually mitigated by lean mixture or retarding the combustion process, i.e., increasing the Crank Angle where 50% of the mixture is burn (CA50). Remarkable benefits of using ultra-lean mixture (i.e., lambda above 2.3) in H2ICEs on NOx mitigation were demonstrated by Zao et al. [30,31] and Lee et al. [30,31]. The large amount of air in the combustion chamber lowers the maximum average charge temperature achieved during the combustion process mitigating the NOx emissions. Besides the high equivalence ratio, several works in the literature demonstrated that similar effects in knock intensity and NOx reduction can be achieved with cooled Exhaust Gas Recirculation (EGR) [14,32,33]. The authors pointed out that lean and highly diluted mixtures with cooled EGR result in nearly NOx-free hydrogen combustion. While effective in mitigating NOx under steady-state conditions, all the strategies presented above have proven to be less successful during fast transient, where NOx production can be limited but not entirely avoided. Therefore, dedicated hydrogen aftertreatment devices are currently being investigated. The Selective Catalyst Reduction (SCR) system is considered one of the most widely used and studied aftertreatment devices, aimed at mitigating NOx in a lean combustion environment. Saravanan et al. mounted a standard SCR in the exhaust pipeline of a H-PFI single cylinder dual fuel compression ignited engine [34]. The authors tested the hydrogen combustion in different engine conditions and demonstrated the

potential of SCR in NOx abatement, achieving a maximum of 75% reduction with marginal reduction in engine efficiency due to the SCR management strategy.

Walter et al. studied the performance of a NOx Storage Catalyst (NSC), focusing on the NOx mitigation efficiency in different operating conditions [35]. The results showed that the NSC can effectively reduce NOx both at low (below 30 °C) and high temperatures (above 320 °C) with an efficiency of 60% and 95%, respectively.

As mentioned above, to mitigate emissions and avoid anomalous combustion, H2ICEs usually operate at ultra-low equivalence ratio [36], thanks to very high intake pressures. In conventional ICEs, the boost pressure is typically provided by a compressor driven by a turbine, where the power needed to drive the compressor is obtained from the exhaust gas. Therefore, the thermodynamic conditions of the exhaust gases are fundamental to ensure the capability to boost the engine. Traditional gasoline combustion relies on stoichiometric air-to-fuel ratio allowing to obtain a sufficiently high exhaust temperature. Several authors in literature have discussed the difficulties of obtaining high boost pressure in H2ICES [37–39]. As previously discussed H2ICEs have to run extremely lean (above 2.3) to ensure low NOx production and avoid combustion anomalies. Nevertheless, the leaner the combustion the lower the enthalpy content of the exhaust gases, resulting in reduced boosting capabilities [37,40]. The low enthalpy content limits also the transients response, which has been addressed with many alternative solutions [41]. Therefore, the management of H2ICEs becomes challenging, particularly during fast transients, where torque request has to be delivered on demand while avoiding combustion anomalies and limit NOx emissions. Nowadays, torque-based controls are the most suitable solution aimed at controlling ICEs and different approaches have been developed throughout the years [42–44]. However, such control strategies have to be modified in order to properly control H2ICEs, but the development and optimization of a control strategy is a complex, time demanding and expensive process. Model-in-the-Loop (MIL) approaches represent a possible solution to limit development costs and perform tests on a detailed engine model capable of simulating both performance and emissions in an accurate way. H2ICEs represent a complex multi-domain system, requiring dedicated modelling for a proper representation of steady-state and dynamic behaviour. Artificial Neural Networks (ANNs) have recently emerged as an accurate and fast solution for the modelling of ICEs [45–47]. Tosso et al. [48] developed a framework aimed at designing a feedforward ANN capable to predict fuel mass, lambda, torque and ignition. Different authors have also studied the capability of ANNs to predict emissions [49–51]. Moreover, Warey et al. [52] exploited convolution neural networks for the prediction of in-cylinder emissions from in-cylinder images of equivalence ratio, temperature, velocity field and turbulence.

In summary, H2ICEs pose unique challenges in the development of control strategies, due to their particular combustion characteristics and dynamic response. Therefore, the need of a well-structured hydrogen engine control system is a key factor to achieve the delicate balance between power delivery and limit abnormal combustion and NOx emission. Moreover, the development of control strategies is an expensive process since many tests on the engine have to be performed, therefore, the MIL approach represents an optimal solution in order to limit the experimental effort.

This paper focuses on the development of a cutting-edge torque-based control strategy for H2ICEs. With the aim of developing a test case for a torque-based controller, an ANN-based dynamic 0-D model of a hydrogen engine has been developed and calibrated. The training database for the 0-D virtual engine calibration has been obtained by running a previously validated 1-D engine model scanning the whole engine operating range. The data collected from the 1-D model, including thermodynamic conditions, the composition of intake and exhaust gases, and combustion metrics, under both steady-state and transient conditions, enabled the description of stochastic phenomena, such as knock occurrence and cycle-to-cycle variability, which have been incorporated in the dynamic 0-D model. Once the simulation environment has been developed, a dedicated CA50-based control structure for hydrogen engines has been designed and implemented. Thanks to a specifically conceived fuel controller, the proposed control strategy follows external torque requests without exceeding the limitations of NOx production and knock, while achieving maximum engine efficiency.

2. Materials and methods

In this section, the development of the engine model and the implementation of the control strategy is presented.

2.1. Virtual engine design

As mentioned before, with the aim of finalizing and testing the proposed engine control strategy, the first step of the activity is focused on the development of a virtual Spark Ignited (SI) engine operated with hydrogen in a dynamic simulation environment. The engine platform selected for this study is a 6-cylinder 3.0 l turbocharged medium duty SI engine specifically modified to operate with hydrogen. Table 2 reports the main engine specifications.

According to the literature on H2ICEs, a complex and integrated intake air management system is crucial to enhance the benefits of hydrogen combustion while preserving the engine from failures. In the engine under study, the boost pressure is generated through a single stage turbocharger with Variable Geometry Turbine (VGT). To properly control the boost pressure while operating the engine at low loads, when the naturally aspirated engine mode is required, the air path also has an integrated throttle body before the intake manifold. Moreover, the engine is equipped with high pressure exhaust gas recirculation (EGR) system. To maximize the benefits of cooled EGR in mitigating NOx and reducing knock, a dedicated EGR cooler is placed before the intake manifold. To fuel the engine with hydrogen, the engine intake has been modified with a twin-injector multi-point PFI system replacing the stock injection system.

Based on the presented engine platform, Millo et al. [53] developed and validated a 1-D engine model through a dedicated 0D/1D/3D-CFD synergetic approach. They demonstrated that a 3D-CFD numerical setup with a detailed chemistry for hydrogen combustion can be used to calibrate a predictive combustion model in the 1-D simulation environment GT Power by Gamma Technologies. The main limitation is the capability of the 3D-CFD model to fully capture cycle-to-cycle variability and combustion anomalies such as pre-ignition, especially when related to hot-spots or hot oil. Using the developed 1-D H2ICE engine model, an extended database describing the hydrogen combustion parameters, engine performance and engine out emissions is obtained. Several conditions of engine speed, relative air-to-hydrogen ratio (λ, defined in Equation (1.1)), CA50, EGRratio (defined in Equation (1.2)) and Brake Mean Effective Pressure (BMEP) have been investigated collecting a wide representation of the engine behaviour. Table 3 summarizes the investigated engine conditions, reporting the range where each engine parameter has been varied.

$$\lambda = A/F\big/_{(A/F)_{st}} \tag{1.1}$$

Table 2
Engine model characteristics.

Parameter	Value
Architecture	3.0 l, 6 cylinders
Compression ratio	12.85
Injection system	Double PFI
Ignition system	Spark Ignited
Charging system	Variable Geometry Turbine
EGR system	Cooled High Pressure EGR

Table 3
Test performed.

Parameter	Range	Step size
Engine speed [RPM]	1000–4000	1000
BMEP [bar]	2 – max achievable BMEP	2
Lambda [/]	2–2.75	0.25
CA50 [° aTDC]	−30 – +30	5
EGR % [%]	0–5	2.5

$$EGR_{rate} = \frac{EGR_{mass}}{Trapped_{mass}} * 100 \quad (1.2)$$

In each simulation, the engine is operated at constant speed, load (BMEP) and λ through two dedicated closed-loop controllers which manage the VGT and throttle (THR) position respectively, following a target BMEP. The hydrogen flow is directly calculated using an injector model to follow the BMEP request at a defined λ. To obtain a comprehensive dataset describing the engine behaviour, the centre of combustion position is varied from very advanced (−30 °aTDC) to extremely retarded (30 °aTDC) in each combination of speed-load- λ. By coupling the air path controllers (VGT and THR) with the injector model, the 1-D virtual engine can automatically adjust the actuators position addressing the input requests while the engine efficiency is changing. Moreover, to fit EGR into the virtual engine and investigate the impact of different EGR rates on hydrogen combustion, a dedicated closed-loop EGR controller is also implemented, and EGR rates sweeps were added to the inputs list.

Since the aim of this work is to design a torque-based control strategy for H2ICEs in a dynamic simulation environment, a fast-running virtual engine is developed and calibrated. Once collected the engine operating parameters and combustion feedback running the 1-D engine model in its entire operating range, to describe the engine behaviour using a 0-D simulation tool, a reduced input-output list is defined. Engine performance, combustion parameters, actuators positions and engine out characteristics were selected and reported in Table 4.

To accurately represent the behaviour of the engine using the reduced dataset (listed in Table 4), dedicated ANNs, one for each selected engine parameter, were designed and calibrated (see Fig. 1). Artificial Neural Networks have been widely used in the literature to model combustion metrics and emissions in internal combustion engines [46,54–57]. A generic diagram of a fully connected ANN is reported in Fig. 2, with an input layer, two hidden layers, an output layer and a set of

Table 4
Parameters extracted from GT Power model.

Class	Variable
Input	RPM
	SA
	THR position
	VGT position
	Fuel mass injected
	EGR Position
Indicated parameters	IMEP
	BMEP
	CA50
	Brake Specific Fuel Consumption (BSFC)
	Maximum in-cylinder pressure (Pmax)
	Maximum in-cylinder temperature (Tmax)
Air path	In-cylinder trapped air mass
	EGR %
	EGR Flow
	Manifold Air Pressure (MAP)
	Boost pressure
	Turbocharger speed
Engine-out conditions	NOx concentration
	Exhaust temperature
	Exhaust mass flow
	Exhaust pressure

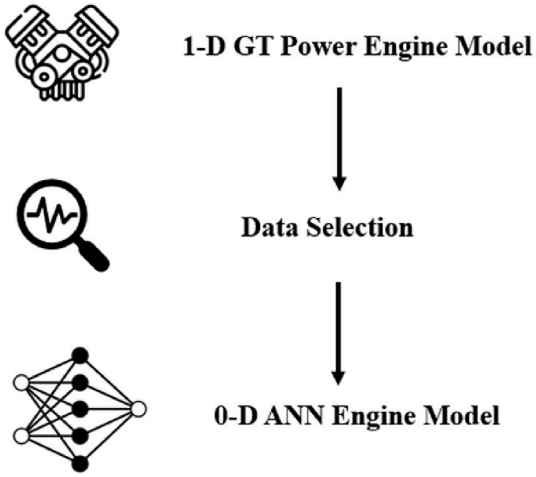

Fig. 1. 0-D engine modelling development and calibration workflow.

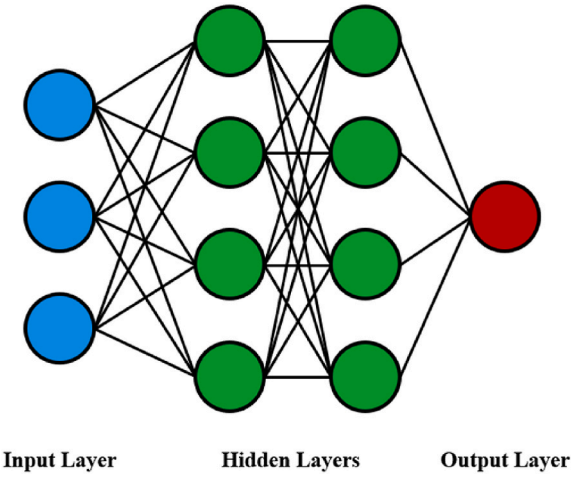

Fig. 2. Generic ANN layout.

neurons per each hidden layer. During the training phase, the ANN learns, from a set of training data, possible non-linear relationships between input and output. In a fully connected ANN, all the neurons of a hidden layer are linked to all the neurons of another one, and each connection relies on a specifically calibrated weight during the training phase starting from a random value. Finally, to validate the prediction capability, the ANN is tested on a reserved dataset of untouched data [58].

In this work, the entire group of neural networks aimed at describing the engine behaviour has been designed and calibrated using the MATLAB *Statistics and Machine Learning Toolbox*. Table 5 reports the generic network structure and data selection methodology used for this work.

To accurately describe the physical connections between each engine parameter, the 0-D engine model integrates all the previously calibrated

Table 5
Generic neural network structure.

Parameter	Value
Number of available data	835
Number of hidden layers	1–2
Number of neurons per hidden layer	10–20
Data division (% training, % validation, % test)	70–15 – 15
Data division method	random
Training algorithm	Levenberg – Marquardt

networks generating an input-output framework, in which each parameter is sequentially calculated. To better clarify this modelling procedure, an example is provided following the steps reported in Fig. 3: the calibration of the network for describing IMEP is obtained using the CA50 and other inputs directly coming from the 1-D model. During the testing procedure, the IMEP network inputs were taken both from a user-selected input list (RPM, SA, VGT, THR, EGR Area and Fuel) and the outputs of previously calibrated networks (CA50 and In-cylinder trapped mass networks). This modelling approach allows to take into consideration all the uncertainties present among the model sections. Fig. 4 shows the 0-D virtual engine model and the entire input-output ANN pattern.

By looking at Fig. 4, the main subsystems of the model can be identified.

- the air path (blue area, a) subsystem, where intake conditions, in-cylinder trapped air and EGR are calculated;
- the combustion subsystem (red area, b), where the combustion related parameters such as CA50, Maximum Pressure Oscillation (MAPO), IMEP are obtained;
- the engine-out (green area, c) subsystem, where NOx emissions and thermodynamic exhaust conditions are produced.

As highlighted in the combustion subsystem in Fig. 4, the BMEP is obtained through a model-based approach. Following the Chen-Flynn friction model [59], the Friction Mean Effective Pressure (FMEP) has been calculated by the calibration of the model coefficients as a function of $P_{cyl,max}$ and $c_{p,m}$, which stand for the maximum in-cylinder pressure and the mean piston speed respectively. The FMEP and the BMEP calculation models used in this work are reported in Equation (1.3) and Equation (1.4) respectively.

$$FMEP = FMEP_{constant} + A * P_{cyl,max} + B * c_{p,m} + C * c_{p,m}^2 \quad (1.3)$$

$$BMEP = IMEP - FMEP \quad (1.4)$$

The 0-D fast running engine model is validated in steady-state operating mode by comparing the output of the 1-D engine model using the same user-defined inputs. The difference between the two models is quantified through the Root Mean Squared Error (RMSE), RMSE percentage (RMSE%) and R-squared calculations.

As it is possible to notice in Table 6, the maximum RMSE% is below 1%, demonstrating the accuracy of the 0-D model for all the considered parameters. It is worth pointing out that, due to the lack of consistent data with high NOx emission, the NOx emissions validation is limited to 2000 ppm.

Fig. 5, Figs. 6 and 7 present the validation and testing process performed for the main parameters. As it is possible to see, all the parameters show an excellent correlation between the 1D GT Power model and the 0D ANN-based model. Lambda shows the worst correlation: this is related to the fact that a small error on the amount of air becomes dominant in the calculus of lambda, since the amount of fuel is externally imposed (equal to that coming from the 1D GT Power model).

Once the 0-D model has been validated in steady state conditions, it has been further modified to be representative of the 1-D model behaviour even during transients. Significant modifications have then been introduced in the air path to increase the accuracy of the proposed 0-D model during transients, as suggested by the literature [60]: intake manifold air dynamics and turbocharger dynamics were added. The intake manifold, positioned between throttle and intake ducts, damps out the pressure oscillations related to step variations in the upstream pressure (due to THR or boost pressure variations). Following the approach proposed by Mezher et al. [61], a specifically calibrated first order dynamic system is used to replicate the intake manifold dynamics. In fact, assuming the manifold pressure equal in every point of the plenum, the filling and emptying of the manifold can be described starting from the continuity equation. The air flow through the valves can be described as a function of the valves area, discharge coefficient and pressure across the valves. Neglecting the dependencies of the discharge coefficient and assuming a constant temperature in the plenum, the pressure behaviour can be described as a first order system where the time constant is proportional to the ratio of manifold and cylinder volumes [62].

Several methodologies aimed at modelling the turbocharger dynamics are reported in the literature [63–65]. The speed variation of the shaft can be described as the net torque applied to the shaft over the overall inertia of the turbocharger [66]. Venson et al. [67] demonstrated that a change in combustion conditions (e.g., as a result of a positive step in the injected fuel) determines an acceleration of the turbocharger that can be represented as a first order system, due to the absence of over-damping and underdamping effects (neglecting combustion inertial effects), linking injected fuel mass with turbocharger speed. This acceleration of the turbocharger can be achieved with a variation in fuel or air mass flow rate, or turbine inlet pressure [67]. The simple identification of the response, gain constant, frequency gain amplitude and phase shift allows the turbocharger dynamics to be accurately represented.

As a result, since detailed modelling of the turbocharger is out of the scope of the presented work, the turbocharger dynamics were obtained through a properly calibrated first order dynamic system, in which the characteristics of the system were mapped as a function of the operating conditions. Additional dynamic effects, such as the fuel and exhaust path transient behaviours, and the thermal effects related to the combustion chamber heating or cooling, were neglected. Fig. 8 shows a comparison between the turbocharger speed coming from the 1-D GT Power model and the first order model in two different conditions of RPM, combustion phasing, lambda, and VGT variation.

Once the dynamic effects were included in the 0-D model, transient validation of the fast-running virtual engine has been performed. To

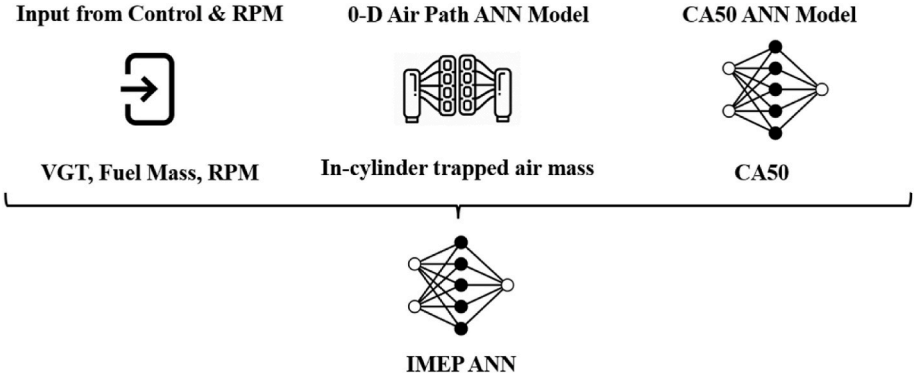

Fig. 3. Example of IMEP ANN test procedure.

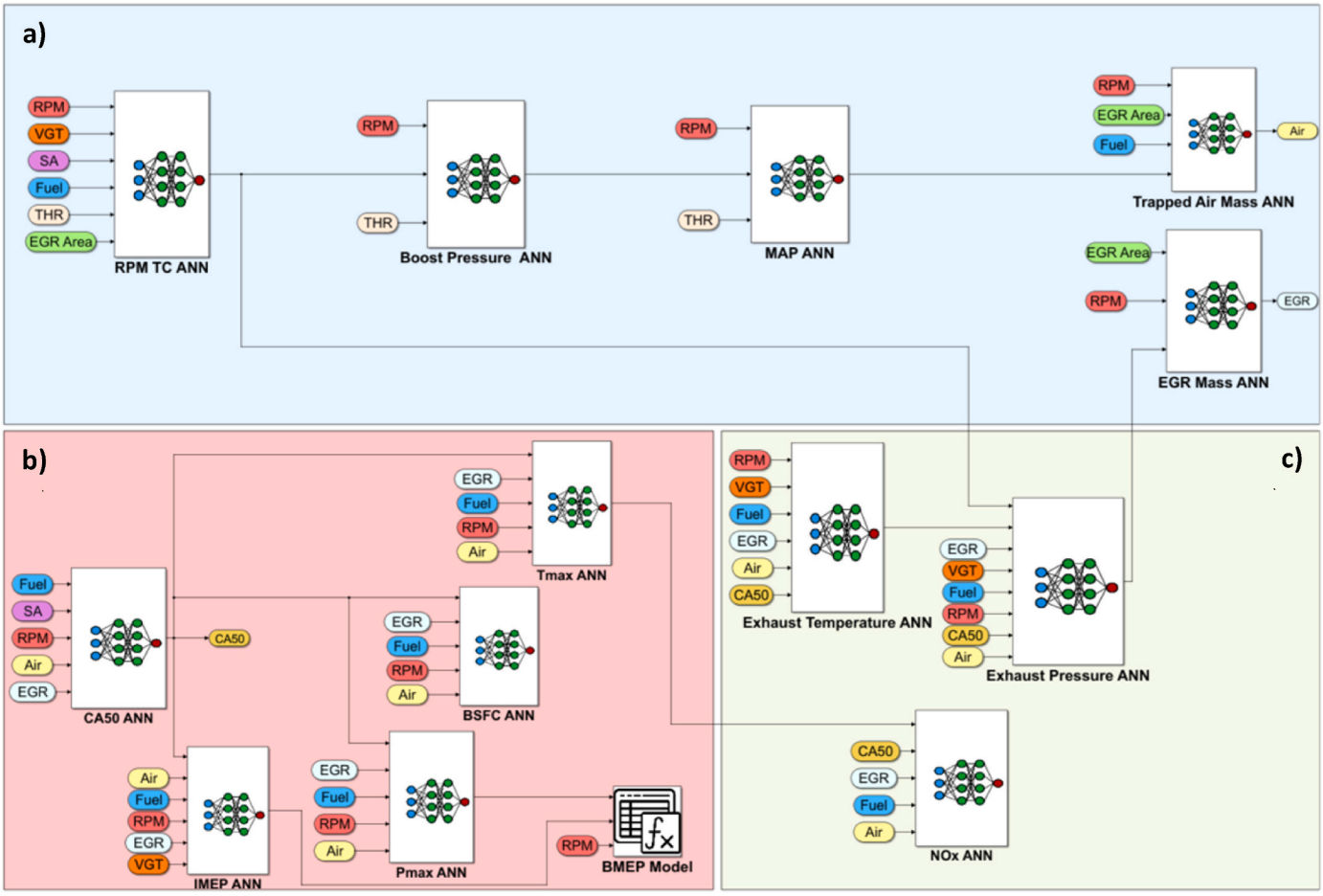

Fig. 4. Schematic representation of the input-output relationship in the 0-D model, air path (a), combustion subsystem (b) and engine-out (c).

Table 6
0-D engine model validation.

Parameter	RMSE	RMSE %	R^2
Turbocharger Speed [RPM]	1077	0.007	0.998
Boost Pressure [bar]	0.022	0.009	0.997
Manifold Pressure [bar]	0.023	0.008	0.998
In-cylinder trapped air mass [mg]	12	0.01	0.996
EGR % [/]	0.053	0.76	0.994
CA50 [°CA]	0.26	0.56	0.996
IMEP [bar]	0.058	0.38	0.997
BSFC [g/kWh]	2.26	0.75	0.994
Pmax [bar]	0.93	0.81	0.998
Tmax [K]	6.57	0.41	0.998
NOx (below 2000 ppm) [ppm]	11	0.56	0.996
Exhaust pressure [bar]	0.05	0.8	0.992
Exhaust temperature [K]	3.5	0.7	0.997
Exhaust Flow [g/s]	0.7	0.35	0.999

achieve this goal, specifically designed simulations were conducted using the 1-D engine model to obtain reference values during transient conditions. Time-based profiles for the following parameters were set: RPM, VGT, THR, fuel mass, and SA. Then, dynamic simulations operating the 0-D fast running virtual engine with the previously defined time-based profiles were conducted.

The comparison between simulations results (generated from the same time-based transient using both 0-D and 1-D models) in terms of air path parameters, combustion parameters, and engine-out conditions are reported in Figs. 9–11, respectively. The accuracy of the 0-D model is evaluated through the Relative Percentage Error calculation defined in Equation (1.5). As it is possible to observe, all the analyzed parameters show relative errors always between ±10% apart during fast transient zones (such as t = 23 s, and t = 150 s, and t = 180 s). Globally, the mean errors always fall between −3 % and 1 % except for the turbocharger speed and NOx where a maximum mean error of −4.9 % occurs.

$$Error\ \% = \frac{1D\ GT\ Power\ Model\ Value - 0D\ ANN\ Model\ Value}{1D\ GT\ Power\ Model\ Value} * 100 \tag{1.5}$$

Since the combustion controller is fed with cycle-based data, to improve the simulation quality the engine stochastic behaviour has been incorporated in the 0-D fast running model. As a matter of fact, according to Azeem et al. [68], in SI H2ICEs significant variations can be observed during the combustion process. As described in the literature, to keep into account the effect of Cycle-to-Cycle Variability (CCV) on engine performance, CCV models were investigated [69,70]. Based on the proposed approaches the ANN-based methodology outlined in Fig. 12 has been adopted. Aforementioned simulations, run using the 1-D engine model, delivered the maps of average CA50 (μ_{CA50}) in different engine conditions, while for CA50 standard deviation (σ_{CA50}) experimental data were used as reference. Then, the associated ANNs (μ_{CA50} and σ_{CA50}) were calibrated and implemented in the 0-D fast running model, allowing the calculation of the Gaussian statistical distribution of CA50 (defined in Equation (1.6)) for the given running condition. A random value can now be selected for each engine cycle out of the CA50 distribution, and considered as the current cycle CA50 for the entire engine model (e.g., for the determination of other metrics).

$$f(x) = \frac{1}{\sqrt{2\pi\sigma_{CA50}^2}} e^{-\frac{(x-\mu_{CA50})^2}{2\sigma_{CA50}^2}} \tag{1.6}$$

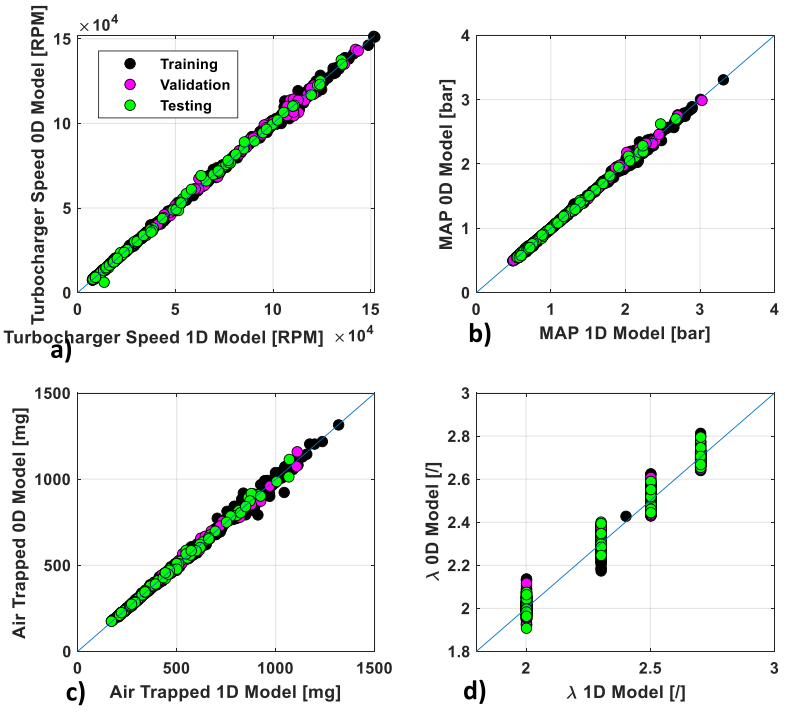

Fig. 5. Testing and validation of air path parameters: turbocharger speed (a), MAP (b), trapped air mass (c), lambda (d).

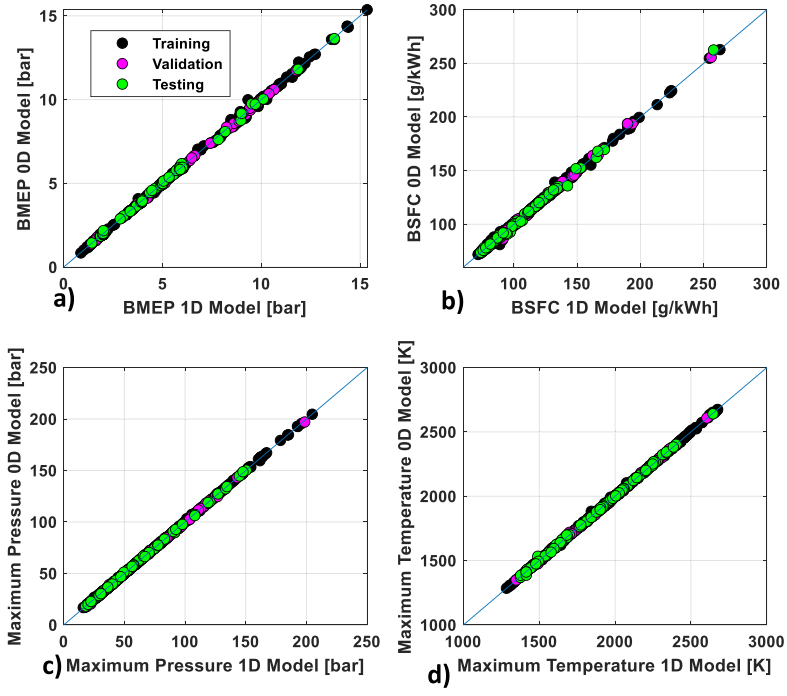

Fig. 6. Testing and validation of combustion parameters: BMEP (a), BSFC (b), Pmax (c), Tmax (d).

Another crucial engine-related stochastic phenomenon, which produces deviations in the combustion metrics, is knock. The final step in the development of the 0-D engine model focused on the knock modelling. To achieve this, the statistical distribution and average value of the knock intensity index were evaluated for each operating condition running the 1-D engine model. In this work, MAPO is considered to represent the knock intensity. Cavina et al. [71] demonstrated how a 0-D predictive knock model can be developed starting form trapped air mass and in-cylinder maximum pressure. Then, following the same approach proposed to model the CCV in the 0-D engine model, two additional

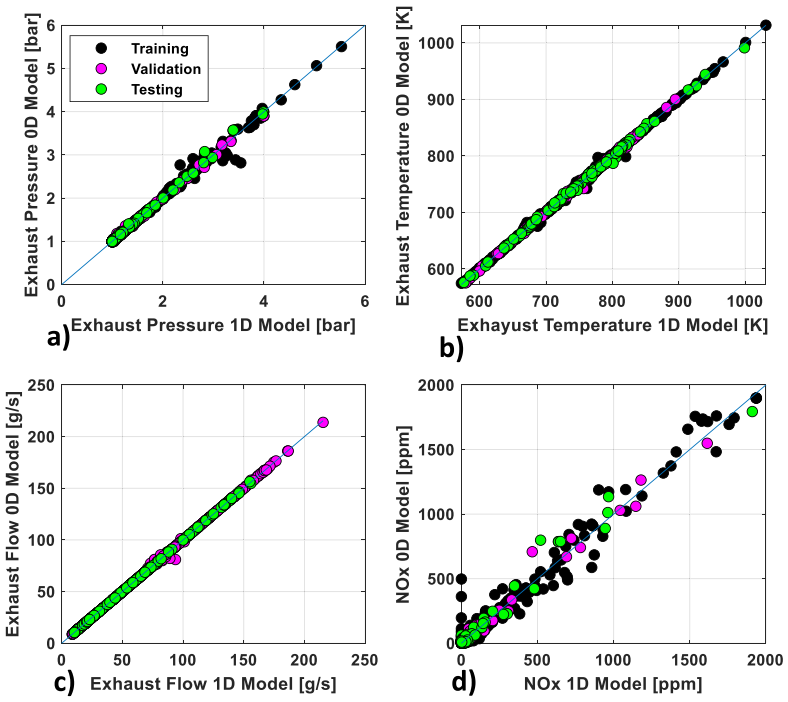

Fig. 7. Testing and validation of engine-out parameters: exhaust pressure (a), exhaust temperature (b), exhaust flow (c), NOx (d).

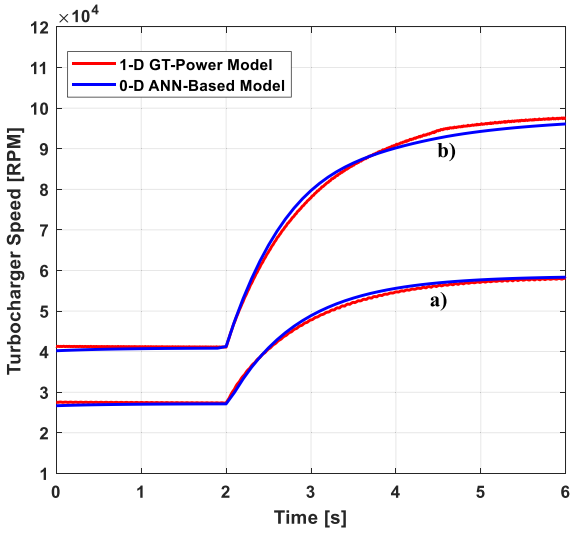

Fig. 8. Turbocharger speed behaviour for the 1-D GT Power model and the first order modelling at 2000 RPM, lambda = 2.3 (a) and 3000 RPM, lambda = 2.2 (b).

ANNs were calibrated using as inputs CA50, hydrogen mass, EGR%, λ, boost pressure, and RPM. It is worth to point out that using the CA50 as one of the inputs of the knock-related ANN, statistical considerations in the modelling of knock events were enabled and partially justified by the CCV. However, as opposed to Pmax and IMEP, the dispersion of MAPO cannot be satisfactorily represented by CA50 alone. This is due to the sensitivity of knock to lambda and temperature spatial distributions [72]. To obtain the current value of MAPO, starting from the outputs of the ANNs, i.e., average MAPO and MAPO standard deviation, a lognormal distribution is defined and a random value within the distribution is selected for each engine cycle. The ANN-based knock model validation is performed operating the 0-D fast running engine model under steady-state conditions (500 cycles were considered). The comparison between the obtained 98th percentile of MAPO (MAPO98) using the 0-D virtual engine and the reference value (coming from the 1-D virtual engine) is reported in Fig. 13. As evident from the results, the knock index calculated through the proposed methodology demonstrates a strong correlation (with R2 equal to 0.968) with the reference MAPO98. This methodology allows the prediction of end-gas knocking, but not of ignition due to hot-spots; however, the proposed approach remains valid, since it allows the generation of a statistical knocking behaviour fundamental for the correct development of the knock control strategy.

2.2. Control strategy model

As documented in the literature, H2ICEs demonstrate maximum benefits in terms of efficiency and NOx reduction when operated with ultra-lean air-fuel mixtures. Nevertheless, standard control strategies have shown limited effectiveness in managing hydrogen combustion across the entire engine operating range, mainly because of its chemical characteristics (high RON and wide flammability range). To bridge this gap, this section describes the developed torque-based engine control strategy for H2ICEs management aimed at mitigating the efficiency-emission trade-off and maximizing the engine reliability. The following subsections describe the main features of the control strategy, which can be summarized in two main parts: fuel and CA50 management (fast-path) and air management (slow-path).

2.2.1. Fuel management

To properly control the engine torque without the risk of abnormal combustions (i.e., knock, misfire, preignition), a dedicated fuel management controller is designed. The goal is to calculate the hydrogen mass to produce the requested torque while considering both reliability and emissions limitations simultaneously. Fig. 14 describes the fuel

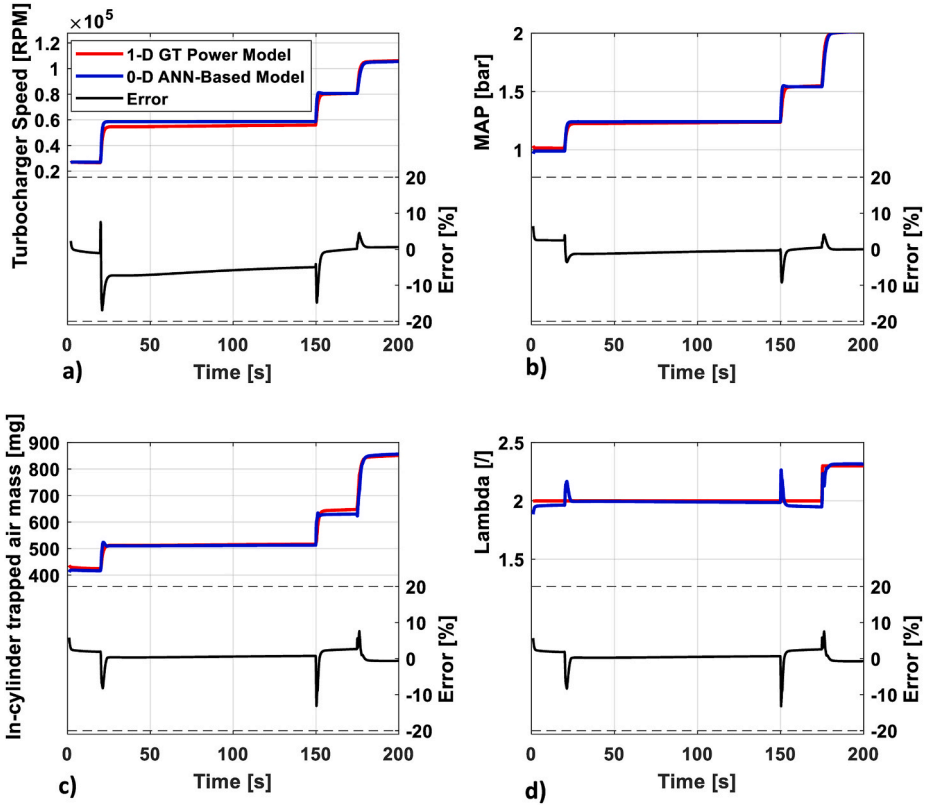

Fig. 9. Validation of the transient behaviour of air path (GT Power reference in red, 0-D ANN-based model in blue and percentage error in black): turbocharger speed (mean error −4.2 %) (a), MAP (mean error −0.3 %) (b), in-cylinder trapped air mass (mean error 0.6 %) (c) and lambda (mean error 0.5 %) (d). (For interpretation of the references to colour in this figure legend, the reader is referred to the Web version of this article.)

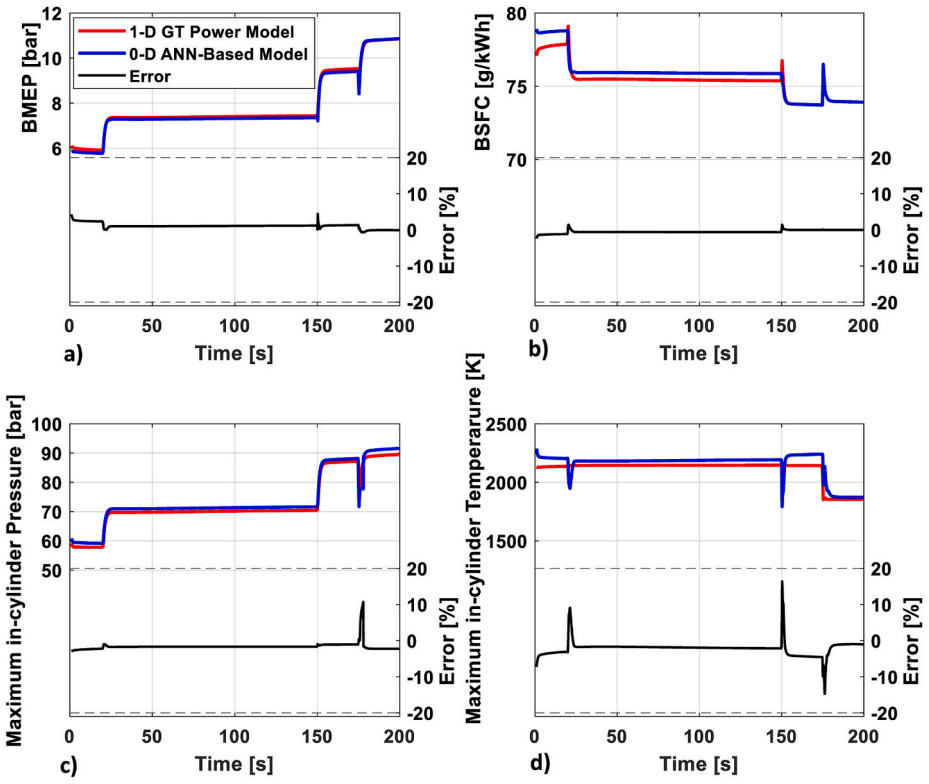

Fig. 10. Validation of the transient behaviour of indicated parameters path (GT Power reference in red, 0-D ANN-based model in blue and percentage error in black): BMEP (mean error 1 %) (a), BSFC (mean error −0.5 %) (b), maximum in-cylinder pressure (mean error −1.6 %) (c) and maximum in-cylinder temperature (mean error −0.2 %) (d). (For interpretation of the references to colour in this figure legend, the reader is referred to the Web version of this article.)

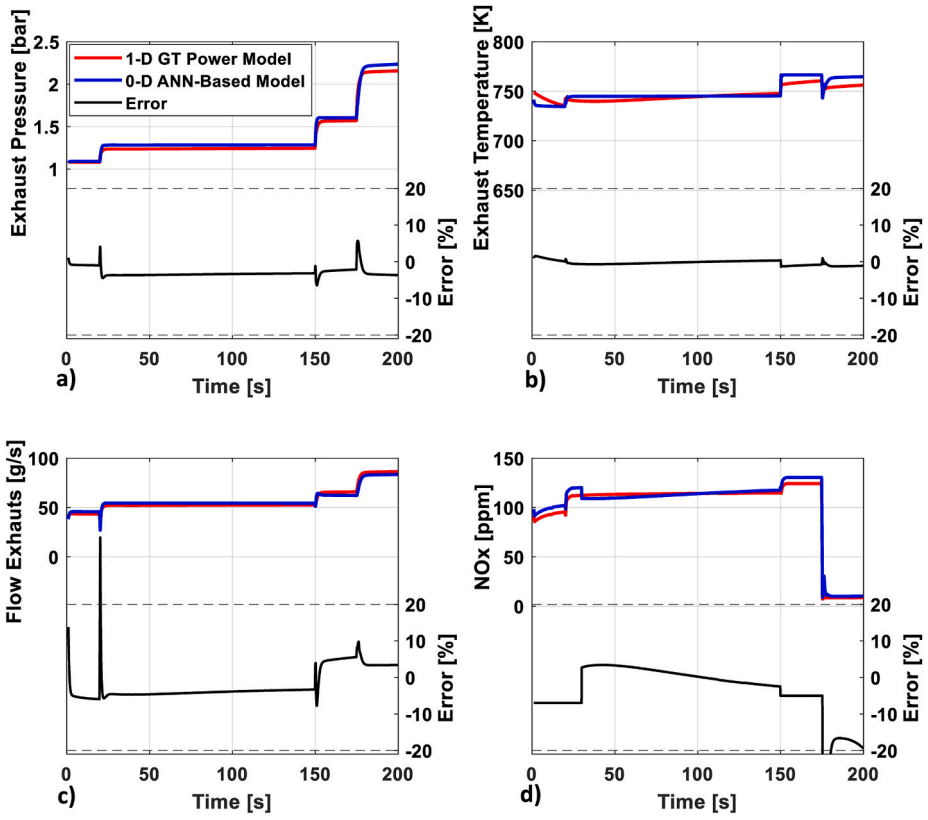

Fig. 11. Validation of the transient behaviour of engine-out (GT Power reference in red, 0-D ANN-based model in blue and percentage error in black): exhaust pressure (mean error −2.9 %) (a), exhaust temperature (mean error −0.3 %) (b), flow exhaust (mean error −2 %) (c) and NOx (mean error −4.6 %) (d). (For interpretation of the references to colour in this figure legend, the reader is referred to the Web version of this article.)

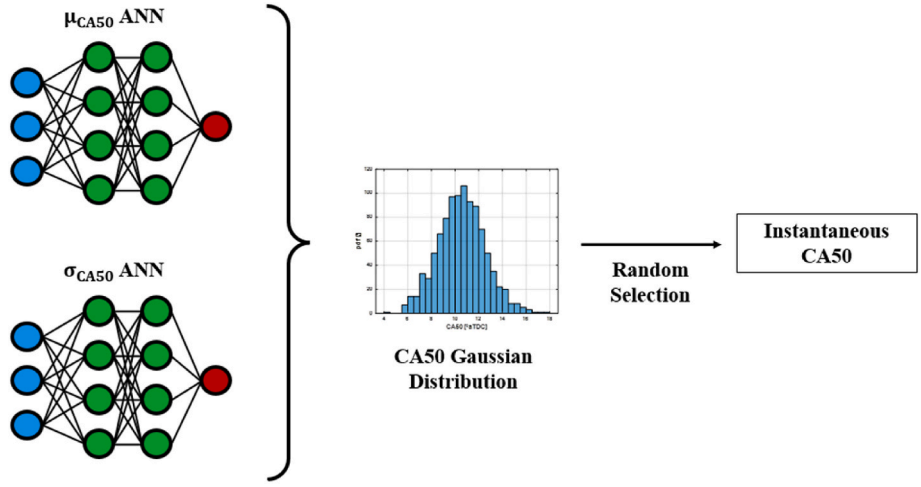

Fig. 12. Procedure for instantaneous CA50 determination.

controller structure and the determination of the fuel request.

The inputs of the fuel controller are the engine load (BMEP) and speed. Starting from this externally defined input, BMEP is converted into an equivalent IMEP request adding engine friction (FMEP). Unlike the model-based approach for FMEP estimation (function of RPM and Pmax) described in the previous section, the engine controller calculates FMEP through a Look-up Table (LuT), as a function of RPM and requested BMEP. It is important to point out that the FMEP reported in Fig. 11 can slightly differ from the instantaneous FMEP (modelled, for each cycle, through Equation (1.3)), mainly because different inputs were used to quantify the load (when the controller calculates the target fuel mass, the instantaneous maximum pressure peak is not available).

Then, the obtained requested IMEP is converted into hydrogen mass trough the "Torque-to-Fuel" (TtF) LuT reported in Fig. 15. The TtF LuT describes the work production (IMEP) of the hydrogen combustion in the engine under study operated at a reference air/fuel ratio and Maximum Brake Torque (MBT) phasing.

However, to address the engine reliability limitations (i.e., optimal CA50 would generate knocking), corrective actions have to be considered. The typical approach, often used in conventional control strategies for SI engines to prevent knocking is to retard the combustion process [14–17] by increasing the CA50. Although effective, this methodology

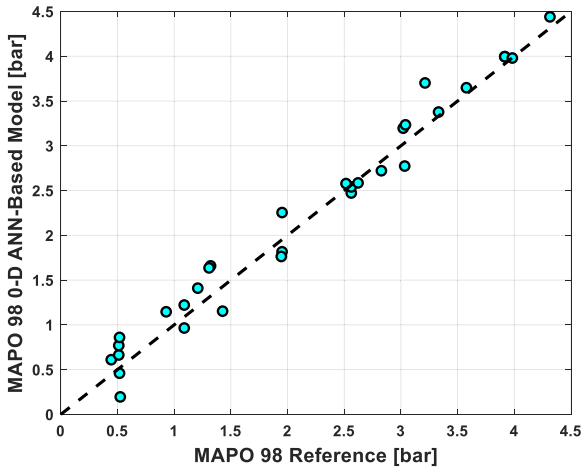

Fig. 13. Reference 98th percentile vs 0-D ANN-Based MAPO 98.

leads to a less efficient combustion, resulting in reduced torque output (if the fuel mass is kept constant). Thus, as reported in Fig. 14, the hydrogen mass coming from the TtF LuT is corrected using an efficiency map (η_{CA50}). Such map, bounded between one and zero ($\eta_{CA50} = 1$ for knock-safe conditions when optimal CA50 can be applied, $\eta_{CA50} < 1$ for knock-limited conditions), increases the hydrogen mass during knock-limited conditions.

Since the goal of the proposed strategy is to maximize the efficiency-emissions trade-off while preserving the engine from failures, two additional fuel limitations were considered. Due to the hydrogen combustion performance sensitivity to the mixture preparation, the proposed limitations were expressed in terms of λ, and then converted into hydrogen mass boundaries (minimum and maximum) in the whole engine operating range. The upper λ limitation prevents misfire, while the lower λ limitation is defined as the minimum λ for addressing knock and NOx emissions limits. As a result, for each engine condition the minimum and maximum λ were calculated and converted in an equivalent allowable hydrogen quantity (using the estimated air flowrate coming from the air controller). In this way, the hydrogen mass is always bounded in the most safe and efficient range.

Bounding the fuel requests generates benefits especially when running fast transients. When a steep decrease in the requested BMEP occurs (from high to low load), the requested hydrogen without saturation would result in a very small quantity. However, due to slower dynamics in the intake manifold with respect to the fuel controller, the air fuel mixture may result too lean, increasing the risk of misfire. Therefore, the injection controller slightly increases the amount of hydrogen avoiding misfire events. It is important to mention that the proposed torque-based strategy manages the CA50 to run at MBT (if possible). As a result, because of the misfire protection, the increase in injected fuel generates extra torque, which leads to a deviation from the requested load. Such a deviation will be instantaneously mitigated decreasing the combustion efficiency by retarding the CA50. This aspect will be discussed in the next paragraph, where the procedure for the identification of the target CA50 is reported.

2.2.2. CA50 management

The second subsystem of the fast path in the torque-based engine control strategy focuses on the determination of the SA. Since mixture quality and dilution have a high impact on flame propagation in hydrogen combustion [33], the conventional SA control strategy for achieving maximum efficiency might result ineffective for proper H2ICEs management. For this reason, an innovative CA50-based control strategy has been developed. Fig. 16 shows the schematic representation of the proposed control structure, which integrates both open and closed

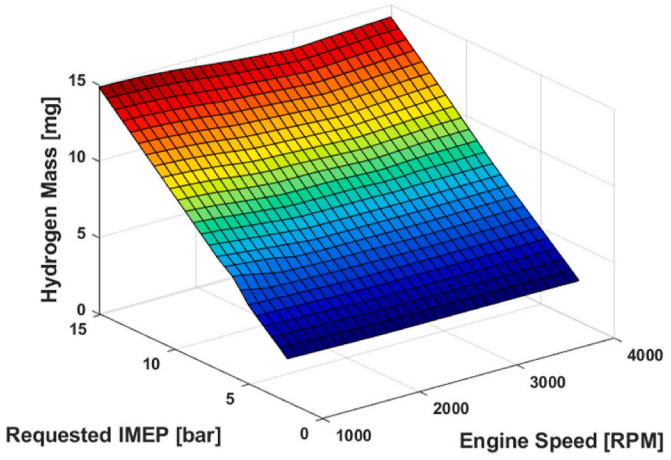

Fig. 15. Torque to fuel map.

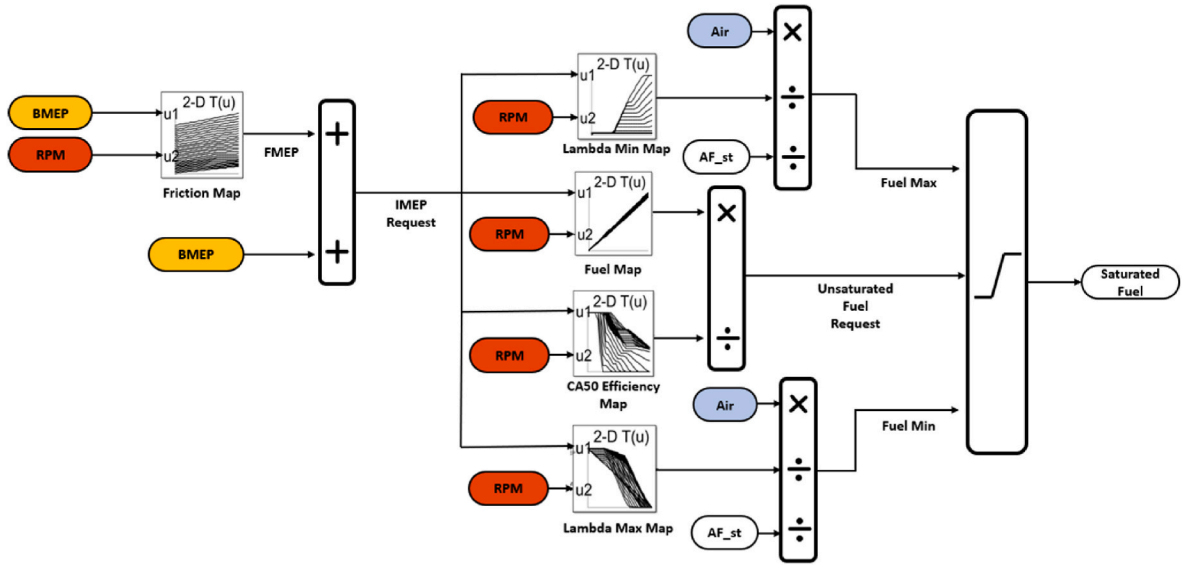

Fig. 14. Hydrogen request determination.

loop contributions in the CA50 target calculation pathway.

The open loop quantity, aimed at defining the CA50 baseline (MBT condition), is calculated as function of RPM, requested IMEP and the estimated λ. Then, the first check on the gross torque production (IMEP) is performed in the "Maximum Available Torque" subsystem. Two different scenarios can be identified:

1. *IMEP requested* $\geq$ *IMEP available:* the engine has no extra torque production capability. CA50 is at MBT and the engine is already producing the maximum available torque using the CA50 baseline (coming from the lookup table) using the previously defined hydrogen mass;
2. *IMEP requested* $<$ *IMEP available:* the engine has extra torque production capability. To align the requested and delivered torque, the engine conversion efficiency is decreased by adjusting CA50 further away from MBT. To quantify the performance degradation related to the combustion phasing, a normalized trend of performance vs phasing ('umbrella curve') is derived from different engine conditions. Fig. 17 shows the trend of normalized IMEP vs ΔCA50 for several engine conditions, and the average normalized umbrella curve used in the "Maximum Available Torque" subsystem. Therefore, the new CA50 is the sum of the baseline CA50 and the penalty contribution from the normalized umbrella curve, ensuring equivalence in terms of the requested and delivered torque.

After obtaining the CA50 target that meets the torque production requirements, to guarantee the stability of the combustion process while respecting the emissions constraints, two additional CA50 limitations were added. These limitations define the range in which CA50 may be located for each engine condition, preserving the engine from abnormal combustions (misfire and knock) and limiting NOx emissions.

As it can be seen in Fig. 16, the closed loop contribution in the CA50 management can be summarized as a reliability-related limitation based on the combustion feedback. For this application, both instantaneous and statistical MAPO and Pmax were selected as reliability-related factors. Direct measurement of in-cylinder pressure can easily provide such feedback [73], but costly measurement toolchain and sensors make this methodology unsuitable for large scale applications. However, in order to reduce costs and promote the diffusion of H2ICE, several works prove that the same information can be estimated through low-cost sensors, such as accelerometers, microphones and piezoelectric washers [26, 74–76]. Fig. 18 shows the subsystem for the statistical knock protection.

As discussed in literature, in hydrogen engines the statistical distribution of MAPO can be represented by a lognormal distribution [77]. As a result, during steady-states (i.e., when engine speed, THR and VGT variations are included within a range of ±5%), the instantaneous

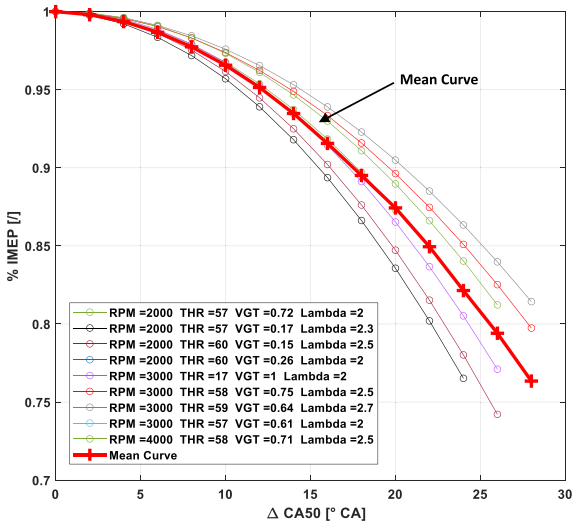

Fig. 17. ΔCA50 vs normalized IMEP for different engine speed, VGT position, THR position and lambda and mean characteristic in red. (For interpretation of the references to colour in this figure legend, the reader is referred to the Web version of this article.)

MAPO is collected in buffers of 50 cycles, and the lognormal distribution parameters are derived. Once obtained the MAPO statistical distribution, the 98th highest percentage of knock intensity (MAPO98) [71], is calculated. Then, to detect knocking, the MAPO98 is compared with a standard knocking threshold as a function of RPM [78]. If the calculated MAPO98 exceeds the defined limit, a properly calibrated Proportional-Integral (PI) controller starts delaying the centre of combustion defined in the previous subsystem. Despite lowering the combustion efficiency, a retarded combustion preserves the engine from severe engine operating conditions.

Beside the statistical knock protection, to shield the engine from heavy knocking (or pre-ignition), instantaneous MAPO is also monitored and the cyclic knock protection is designed. By comparing cyclic MAPO with a user-defined threshold (the engine reliability is the main driver for selecting the limit), heavy knock events can be detected. Fig. 19 highlights the heavy knock protection subsystem. If the cyclic MAPO exceeds the limit, a time-based CA50 delay (in this case a ramp is considered) increases the lower bound in the CA50 range. A retarded CA50 lowers the peak in the bulk temperature and hinders the formation of combustion chamber condition that can lead to abnormal and

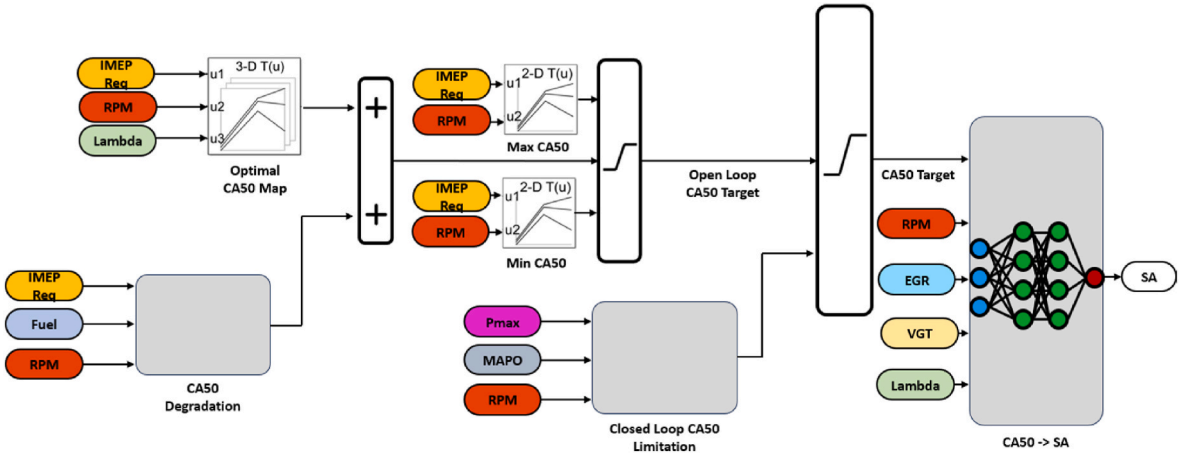

Fig. 16. Target CA50 determination.

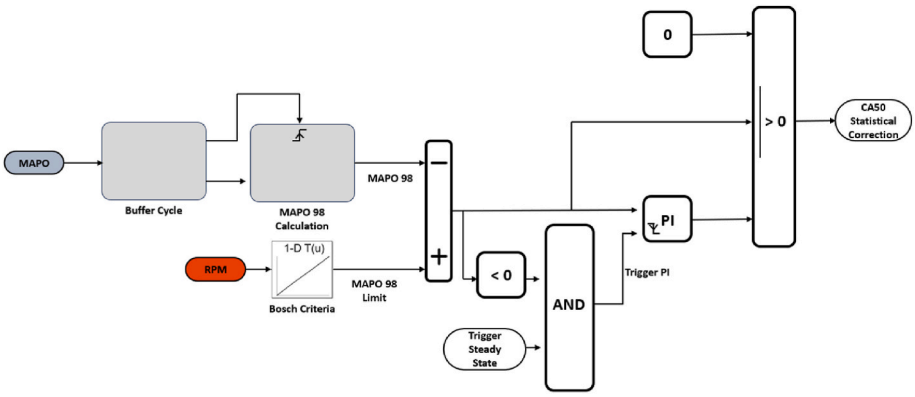

Fig. 18. Statistical MAPO control.

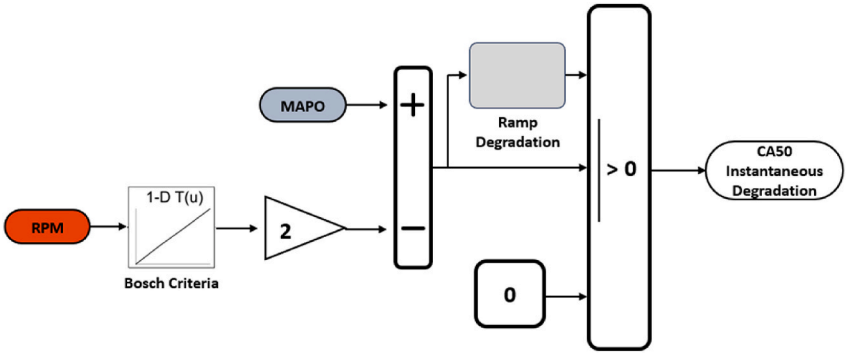

Fig. 19. Instantaneous MAPO control.

potentially dangerous combustion events. It is important to mention that both statistical and cyclic knock protections were integrated in the same subsystem and contribute to CA50 target determination.

As already remarked, to obtain very high efficiency, H2ICEs are characterized by high compression ratio and very low equivalence ratio. The combination of these two aspects leads to an increase in boost pressure, resulting in extremely high in-cylinder pressure peaks during combustion. As a result, Pmax might reach values very close to the mechanical reliability threshold of the engine. For this reason, Pmax protection is also designed. Since Pmax is highly correlated with CA50 and its statistical cycle-to-cycle behaviour, following the same knock-related approach, a statistical monitoring on average Pmax is implemented (potential issues generated by excessive peak pressure does not require statistical manipulation). If the average Pmax in the analyzed buffer overcomes the user-defined reliability threshold, the Pmax protection progressively retards CA50 preserving the engine from mechanical failures.

Finally, the calculated CA50 target (open loop and closed loop contributions are integrated) is converted into a corresponding SA by using a previously calibrated ANN as function of CA50, engine speed, VGT, EGR, and air-to-fuel ratio.

2.2.3. *Air management*

The last control strategy subsystem focuses on air delivery management. As reported in Fig. 17, where the VGT management is presented, after defining the boost requirements based on the engine operating conditions (2-D lookup table is previously calibrated using the outcome of the 1-D engine model), the actuators position in the air path are defined. The same control structure is also implemented for THR management. To properly control boost and manifold pressure based on actual feedback (coming from the 0-D engine model), VGT and THR are managed coupling both open and closed loop inputs. Following the example shown in Fig. 20, the open loop position of the actuator (VGT in this case) is calculated form a 2-D lookup table, and then the position is corrected with a properly calibrated PI controller, which slightly changes the position to meet the requested boost. As regards EGR management, the open loop position of the EGR valve is calculated by means of a 2D look up table, as a function of engine speed and requested IMEP. In this case, the EGR position is controlled only in open loop.

3. Results and discussion

This section describes the results obtained by coupling the 0-D fast running virtual engine with the developed torque-based engine control strategy. To properly evaluate the performance of the engine controller (to deliver the requested torque and control the combustion process), the inputs for each simulation were defined as time-based RPM and BMEP demanded profiles. Both fast transient and steady-state conditions were investigated, and all the engine parameters were monitored.

First findings were obtained by the analysis of the air system behaviour. Fig. 21 a) and b) show the comparison between target and actual values in boost pressure and MAP, respectively. As confirmed by the percentage error evaluation (black dashed lines in Fig. 21), the developed strategy can accurately control the air request for engine management.

It is noticeable that due to the physical behaviour of the engine intake (turbocharger and intake manifold dynamics), when steep variations in boost pressure are requested (t = 5s, and t = 15s), the air controller is not able to keep the pressure close to its target value. Such deviations are generated by the typical behaviour of PI controllers during fast transients. As a matter of fact, the boost requests trace a step variation, which cannot be followed instantaneously due to air dynamics. This results in a slight overshoot in the actual boost pressure, as soon as it exceeds the target. This aspect can be controlled introducing a

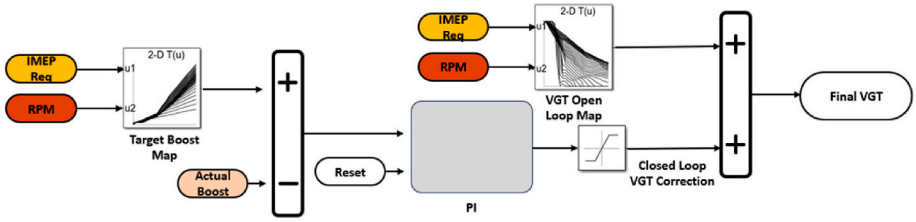

Fig. 20. Closed loop determination of VGT.

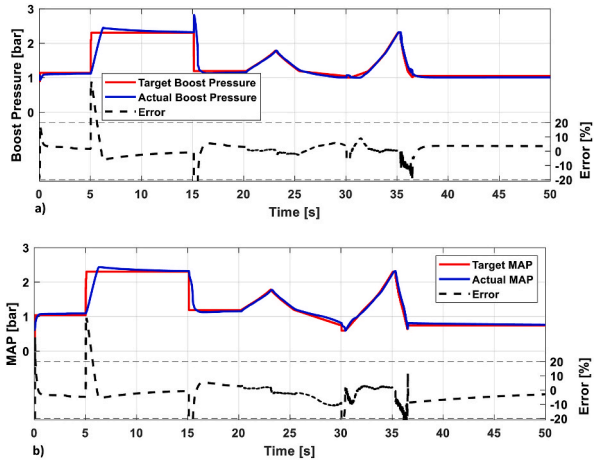

Fig. 21. Boost (a) and MAP (b) comparison between targets (in red) and actual values (in blue) and percentage error (in black). (For interpretation of the references to colour in this figure legend, the reader is referred to the Web version of this article.)

rate limiter on the requested boost pressure.

It is observed that due to the reliability and emissions limitations considered in the control strategy, the λ and CA50 values might not exceed safety thresholds during steep increases or decreases in load requests (t = 5s, and t = 15s). As a result, the hydrogen quantity is bounded and CA50 is adjusted accordingly. Figs. 22 and 23 show the behaviour of the hydrogen mass and CA50 controllers, respectively.

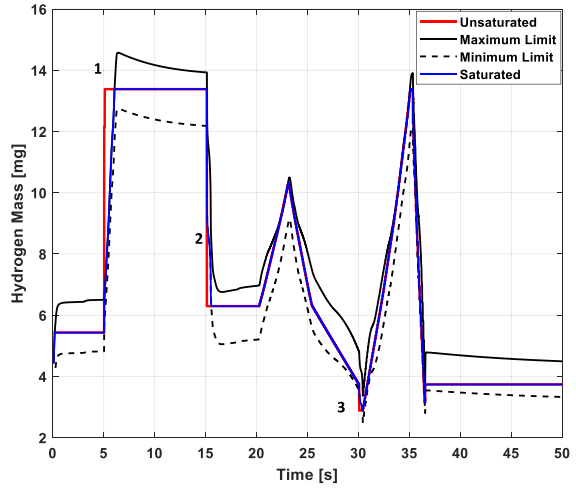

Fig. 22. Fuel comparison between unsaturated (in red), saturated (in blue) and minimum (in black dotted line) and maximum (in black solid line) limits. (For interpretation of the references to colour in this figure legend, the reader is referred to the Web version of this article.)

By looking at the fuel mass controller separately (Fig. 19), the actual hydrogen mass is well aligned with the target, except during fast load transients (in those portions a saturation is present). In particular, saturation takes places in point 1 to avoid an excessively riche mixture, due to slow air dynamics, and points 2 and 3 avoiding too-lean mixtures. Overall, the fuel controller can effectively manage the load demand by controlling the hydrogen injected quantity (i.e., torque) complying with knock/NOx and misfire limitations.

Fig. 23 shows both the target and actual CA50 values, clearly highlighting the characteristic cyclic variations of SI combustion due to the CCV, while the average actual value closely aligns with the target. Furthermore, during steep load decreasings at t = 15s and t = 35s, the influence of misfire protection becomes predominant in defining the target CA50. As extensively explained in the previous section, when the engine has extra torque production capability, both fuel and combustion controllers cooperate to produce the requested torque: the misfire protection limits the minimum hydrogen injected quantity and the combustion controller delays the CA50 to keep the load at the requested value.

It is important to mention that, during the previously shown simulations, the engine is always operating in knock-safe conditions. As a result, the developed knock protection strategy is inactive: to test its impact on CA50 management, the engine is operated under knocking conditions while running the same load-speed profile. Fig. 24 shows the contribution of knock protections on CA50 management while running the engine in unsafe conditions.

As previously described, the knock protection operates using both instantaneous and statistical knock indexes (MAPO and MAPO98). After collecting enough engine cycles under steady-state conditions and calculating the statistical knock index, i.e., MAPO98, the knock protection strategy intervenes when MAPO98 exceeds the user-defined MAPO98 threshold. The protection progressively retards the

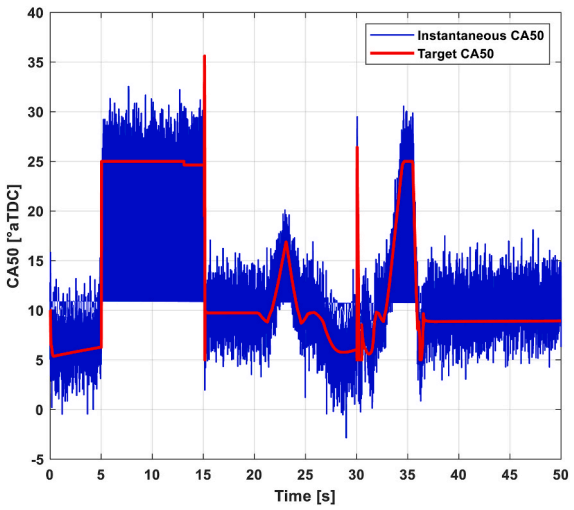

Fig. 23. CA50 instantaneous (in blue) and target (in red). (For interpretation of the references to colour in this figure legend, the reader is referred to the Web version of this article.)

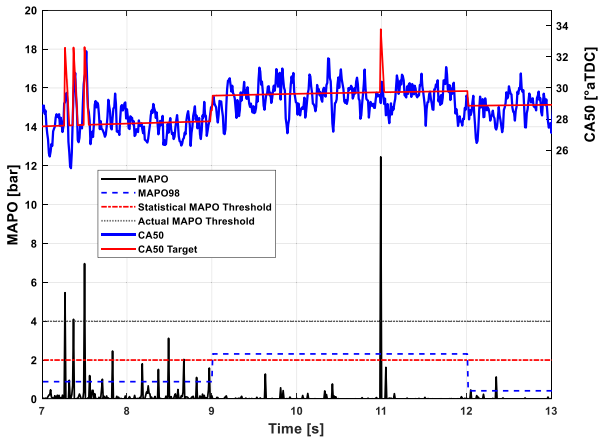

Fig. 24. Instantaneous MAPO (in black), MAPO 98 (in blue dotted), instantaneous MAPO threshold (in dotted grey), statistical MAPO threshold (in dotted red), instantaneous CA50 (in blue) and target CA50 (in red). (For interpretation of the references to colour in this figure legend, the reader is referred to the Web version of this article.)

combustion process (the PI controller increases the CA50 target) until the statistical index exceeds the threshold. An example of such situation is reported in Fig. 21 from t = 9 s to t = 12 s. Then, after operating retarded combustion, the MAPO98 returns below the safety threshold, the impact of the statistical knock protection ends and the target CA50 is reinstated. As mentioned before, both instantaneous and statistical knock protection are enabled. Fig. 24 shows the contribution of instantaneous knock protection when the MAPO index of a given cycle exceeds the user-defined reliability threshold (4 bar in this case). After each detected conditions, to preserve the engine from consecutive sever knocking, the following engine cycles were characterized by delayed CA50 (t = 7.2s, t = 7.3s, t = 7.5s, and t = 11s).

To verify the performance of the developed engine controller following user-defined torque profiles, Fig. 25 compares requested (red curve) and delivered (blue curve) BMEP. As it can be noticed, the proposed torque-based controller can effectively manage the engine following the load profile within a range of ±5% BMEP error and a maximum derivative BMEP deviation of 3.75 bar/s. By the analysis of the engine behaviour operating with the proposed engine management strategy, the observed lag in torque production is strictly related to the air path dynamics (turbocharger). When a steep increase in load is requested (t = 5s), due to the time-to-boost delay (i.e., turbo-lag), the hydrogen injected quantity (and then BMEP) is bounded until a proper amount of air is available according to the lower λ limit (t = 6s).

By looking at Fig. 25, it is important to highlight remarkable BMEP variations at high load (from t = 7s to t = 15s). Such behaviour can be easily explained by the high sensitivity to CCV when the engine is operated with retarded CA50 (knock-limited conditions). As reported in Fig. 17, the normalized umbrella curve shows a steeper performance degradation region when running the engine with retarded combustion, compared to the area near MBT [79].

Fig. 26 shows the impact of the designed knock protections and NOx emission limitations. As a matter of fact, retarded CA50 and low-lambda limitation lower the bulk gas temperature during combustion and then generate near-zero NOx emissions at high load (from t = 7s to t = 15s) [80–83]. Finally, due to the relatively low boost pressure and the previously described engine behaviour at high load, the Pmax (Fig. 26 a)) is always well-below the user-defined reliability threshold (equal to 140 bar). As a result, the Pmax protection is never triggered. However, the presence of this feature might become crucial when higher boost and compression ratios are selected.

4. Conclusions & future developments

This paper describes the development of a torque-based control strategy to manage hydrogen combustion in hydrogen fuelled internal combustion engines (H2ICEs). The controller is able to deliver the requested torque in safe, clean and reliable conditions. Moreover, due to the torque-based structure, the presented engine controller can be adopted for the control of complex zero-emission hybrid powertrains (series/parallel) based on H2ICE, where the overall torque request can be split between thermal and electric power sources.

With the aim of performing software in the loop testing of the combustion controller, a fast running 0-D Artificial Neural Network (ANN)-based virtual engine is designed and calibrated starting from a previously calibrated 1D engine model. To obtain the dataset for the dynamic 0-D engine model development, a wide set of simulations running the detailed 1-D virtual engine were performed. Then, several ANNs representing the dynamic of the 0-D virtual engine were trained and tested. The engine simulator demonstrated good accuracy on replicating the engine behaviour both in steady-state and transient conditions compared to the 1-D engine model.

At the same time, the torque-based control strategy is designed in two main subsystems: fuel and 50% burned mass crank angle (CA50) management, and air management. The first subsystem mainly consists of.

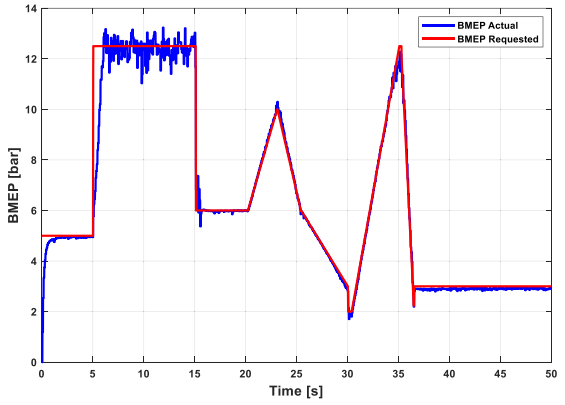

Fig. 25. BMEP behaviour under a transient simulation.

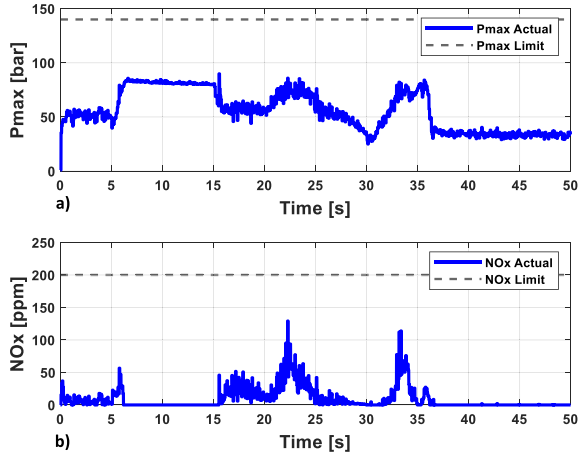

Fig. 26. Pmax (a) and NOx (b) behaviours under a transient simulation.

- fuel request management including knock, nitrogen oxides (NOx) and misfire protections;
- CA50 target definition and management including knock, NOx and misfire protections.

The second subsystem manages the actuators positions following the air request. Boost pressure and manifold air pressure were controlled with both dedicated open and closed loop contributions.

To quantify the benefits of the developed control strategy on engine controllability and emissions mitigation while operating on hydrogen, dynamic user-defined engine conditions based on Brake Mean Effective Pressure (BMEP) and engine speed were tested using the developed engine controller. The analysis of the results highlighted the potential of the control structure in hydrogen combustion effective management. Load requests (BMEP) can be followed within a ±5% both steady-state and transient conditions (maximum BMEP gradient deviation of 3.75 bar/s). Moreover, due to proper control of the target equivalence ratio and CA50 in all the tested operating points, the engine is always operated in knock-safe conditions, and NOx emissions were effectively mitigated. Since relatively low boost pressure values were obtained at high load, maximum in-cylinder pressure is also kept well-below the user-defined reliability limit. The innovative controller here developed can improve the widespread of H2ICEs, enhancing hydrogen-based mobility since it allows to properly deliver the requested torque in a safe, clean and reliable manner.

Future developments of this work are mainly focused on NOx emission control through a dedicated hydrogen-based Selective Catalyst Reduction (SCR) model. Moreover, since cold-start management represents one of the most critical aspects in emissions mitigation operating ICE, the thermal dynamics of the exhaust line will be modelled and added in the 0-D virtual engine. A dedicated cold-start engine management strategy will also be designed and calibrated. In this framework, the developed control strategy will be further improved by adding a hydrogen consumption minimization strategy (considering both hydrogen quantity for combustion and for SCR management). Furthermore, the control strategy will be optimized, introducing other dependencies for the identification of the optimal CA50 (i.e., air temperature, humidity).

Funding

Research funded by Ministero dell'Istruzione, dell'Università e della ricerca (MIUR) (2020R92Y3Z).

CRediT authorship contribution statement

Pier Paolo Brancaleoni: Data curation, Investigation, Methodology, Validation, Visualization, Writing – original draft, Software. **Enrico Corti:** Conceptualization, Funding acquisition, Investigation, Methodology, Project administration, Resources, Supervision, Writing – review & editing. **Vittorio Ravaglioli:** Conceptualization, Investigation, Methodology, Supervision, Writing – review & editing. **Davide Moro:** Conceptualization, Methodology, Resources, Supervision, Writing – review & editing. **Giacomo Silvagni:** Conceptualization, Software, Supervision, Visualization, Writing – review & editing.

Declaration of competing interest

The authors declare the following financial interests/personal relationships which may be considered as potential competing interests: Enrico Corti, Vittorio Ravaglioli, Davide Moro reports financial support was provided by Ministry of Education and Merit. If there are other authors, they declare that they have no known competing financial interests or personal relationships that could have appeared to influence the work reported in this paper.

References

[1] 'Reducing carbon emissions: EU targets and policies | Topics | European Parliament'. Accessed: February. 12, 2024. [Online]. Available: https://www.europarl.europa.eu/topics/en/article/20180305STO99003/reducing-carbon-emissions-eu-targets-and-policies.
[2] European Green Deal - Consilium'. Accessed: February. 12, 2024. [Online]. Available: https://www.consilium.europa.eu/en/policies/green-deal/.
[3] Xing H, Stuart C, Spence S, Chen H. Alternative fuel options for low carbon maritime transportation: pathways to 2050. J Clean Prod May 2021;297:126651. https://doi.org/10.1016/j.jclepro.2021.126651.
[4] '[2102.00439] Fuels of the Future for Renewable Energy Sources (Ammonia, Biofuels, Hydrogen)'. Accessed: February. 16, 2024. [Online]. Available: https://arxiv.org/abs/2102.00439. Pages 1-30.
[5] Verhelst S. Recent progress in the use of hydrogen as a fuel for internal combustion engines. Int J Hydrogen Energy Jan. 2014;39(2):1071–85. https://doi.org/10.1016/j.ijhydene.2013.10.102.
[6] Dimitrova Z, Nader WB. PEM fuel cell as an auxiliary power unit for range extended hybrid electric vehicles. Energy Jan. 2022;239:121933. https://doi.org/10.1016/j.energy.2021.121933.
[7] de Almeida SCA, Kruczan R. Effects of drivetrain hybridization on fuel economy, performance and costs of a fuel cell hybrid electric vehicle. Int J Hydrogen Energy Nov. 2021;46(79):39404–14. https://doi.org/10.1016/j.ijhydene.2021.09.144.
[8] Sáinz D, et al. Conversion of a gasoline engine-generator set to a bi-fuel (hydrogen/gasoline) electronic fuel-injected power unit. Int J Hydrogen Energy Oct. 2011;36(21):13781–92. https://doi.org/10.1016/j.ijhydene.2011.07.114.
[9] Sopena C, Diéguez PM, Sáinz D, Urroz JC, Guelbenzu E, Gandía LM. Conversion of a commercial spark ignition engine to run on hydrogen: performance comparison using hydrogen and gasoline. Int J Hydrogen Energy Feb. 2010;35(3):1420–9. https://doi.org/10.1016/j.ijhydene.2009.11.090.
[10] Arsie I, et al. A new generation of hydrogen-fueled hybrid propulsion systems for the urban mobility of the future. Energies Dec. 2023;17(1):34. https://doi.org/10.3390/en17010034.
[11] Nabi MN, Rasul MG, Arefin MA, Akram MW, Islam MT, Chowdhury MW. Investigation of major factors that cause diesel NOx formation and assessment of energy and exergy parameters using e-diesel blends. Fuel May 2021;292:120298. https://doi.org/10.1016/j.fuel.2021.120298.
[12] Saravanan S, Nagarajan G, Anand S, Sampath S. Correlation for thermal NOx formation in compression ignition (CI) engine fuelled with diesel and biodiesel. Energy Jun. 2012;42(1):401–10. https://doi.org/10.1016/j.energy.2012.03.028.
[13] Luo Q, et al. Experimental investigation of combustion characteristics and NOx emission of a turbocharged hydrogen internal combustion engine. Int J Hydrogen Energy Feb. 2019;44(11):5573–84. https://doi.org/10.1016/j.ijhydene.2018.08.184.
[14] Heffel J. NOx emission reduction in a hydrogen fueled internal combustion engine at 3000 rpm using exhaust gas recirculation. Int J Hydrogen Energy Nov. 2003;28(11):1285–92. https://doi.org/10.1016/S0360-3199(02)00289-6.
[15] Sharma P, Dhar A. Advances in hydrogen-fuelled compression ignition engine. In: Singh AP, Agarwal RA, Agarwal AK, Dhar A, Shukla MK, editors. Prospects of alternative transportation fuels. Singapore: Springer; 2018. p. 55–78. https://doi.org/10.1007/978-981-10-7518-6_5. Energy, Environment, and Sustainability.
[16] Karim GA. Hydrogen as a spark ignition engine fuel. Int J Hydrogen Energy 2003;(5).
[17] Pielecha I, Merkisz J, Urbański P, Gallas D, Andrych-Zalewska M. A numerical study of the effect of hydrogen fuelled turbulent jet ignition engine. In: Presented at the SAE powertrains, fuels & lubricants conference & exhibition; Aug. 2022. https://doi.org/10.4271/2022-01-1007. 2022-01–1007.
[18] Homan HS, Reynolds RK, De Boer PCT, McLean WJ. Hydrogen-fueled diesel engine without timed ignition. Int J Hydrogen Energy Jan. 1979;4(4):315–25. https://doi.org/10.1016/0360-3199(79)90006-5.
[19] Kim C, Park C, Kim Y, Choi Y. Power characteristics with different types of turbochargers for lean boosted hydrogen direct injection engine in NOx-free operation. Heliyon Mar. 2023;9(3):e14186. https://doi.org/10.1016/j.heliyon.2023.e14186.
[20] Lou D, et al. Investigation of the combustion and particle emission characteristics of a GDI engine with a 50 MPa injection system. Fuel May 2022;315:123079. https://doi.org/10.1016/j.fuel.2021.123079.
[21] Yip HL, et al. A review of hydrogen direct injection for internal combustion engines: towards carbon-free combustion. Appl Sci Jan. 2019;9(22):22. https://doi.org/10.3390/app9224842.
[22] Wang L, et al. The effect of hydrogen injection parameters on the quality of hydrogen–air mixture formation for a PFI hydrogen internal combustion engine. Int J Hydrogen Energy Sep. 2017;42(37):23832–45. https://doi.org/10.1016/j.ijhydene.2017.04.086.
[23] Khalid AH, et al. Hydrogen port fuel injection: review of fuel injection control strategies to mitigate backfire in internal combustion engine fuelled with hydrogen. Int J Hydrogen Energy May 2024;66:571–81. https://doi.org/10.1016/j.ijhydene.2024.04.087.
[24] Lai F, Sun B, Wang X, Zhang D, Luo Q, Bao L. Research on the inducing factors and characteristics of knock combustion in a DI hydrogen internal combustion engine in the process of improving performance and thermal efficiency. Int J Hydrogen Energy Mar. 2023;48(20):7488–98. https://doi.org/10.1016/j.ijhydene.2022.11.091.
[25] Li Y, Gao W, Li Y, Fu Z, Zou J. Numerical investigation on combustion and knock formation mechanism of hydrogen direct injection engine. Fuel May 2022;316:123302. https://doi.org/10.1016/j.fuel.2022.123302.

[26] Szwaja S, Bhandary K, Naber J. Comparisons of hydrogen and gasoline combustion knock in a spark ignition engine. Int J Hydrogen Energy Dec. 2007;32(18):5076–87. https://doi.org/10.1016/j.ijhydene.2007.07.063.
[27] Kee S-S, Shioji M, Mohammadi A, Nishi M, Inoue Y. Knock characteristics and their control with hydrogen injection using a rapid compression/expansion machine. SAE Trans 2007;116:217–26.
[28] Lanz W. Module 3: hydrogen use in internal combustion engines. Hydrog. Fuel 2001:2–3.
[29] Onorati A, et al. The role of hydrogen for future internal combustion engines. Int J Engine Res Apr. 2022;23(4):529–40. https://doi.org/10.1177/14680874221081947.
[30] Zhao F, Sun B, Yuan S, Bao L, Wei H, Luo Q. Experimental and modeling investigations to improve the performance of the near-zero NOx emissions direct-injection hydrogen engine by injection optimization. Int J Hydrogen Energy Sep. 2023. https://doi.org/10.1016/j.ijhydene.2023.09.039. S0360319923046037.
[31] Lee S, Kim G, Bae C. Effect of mixture formation mode on the combustion and emission characteristics in a hydrogen direct-injection engine under different load conditions. Appl Therm Eng Jun. 2022;209:118276. https://doi.org/10.1016/j.applthermaleng.2022.118276.
[32] Guo H, Zhou S, Zou J, Shreka M. A numerical investigation on de-NOx technology and abnormal combustion control for a hydrogen engine with EGR system. Processes Sep. 2020;8(9):9. https://doi.org/10.3390/pr8091178.
[33] Thomas Koch D, Sousa A, Bertram D. H2-Engine operation with EGR achieving high power and high efficiency emission-free combustion. presented at the 2019 JSAE/SAE Powertrains, Fuels and Lubricants Dec. 2019. https://doi.org/10.4271/2019-01-2178. 2019-01–2178.
[34] Saravanan N, Nagarajan G. An insight on hydrogen fuel injection techniques with SCR system for NOX reduction in a hydrogen–diesel dual fuel engine. Int J Hydrogen Energy Nov. 2009;34(21):9019–32. https://doi.org/10.1016/j.ijhydene.2009.08.063.
[35] Walter S, Hagen G, Koch D, Geißelmann A, Moos R. On the suitability of NOx-storage-catalysts for hydrogen internal combustion engines and a radio frequency-based NOx loading monitoring. Top Catal Aug. 2023;66(13–14):964–72. https://doi.org/10.1007/s11244-022-01727-x.
[36] Sementa P, de Vargas Antolini JB, Tornatore C, Catapano F, Vaglieco BM, López Sánchez JJ. Exploring the potentials of lean-burn hydrogen SI engine compared to methane operation. Int J Hydrogen Energy Jul. 2022;47(59):25044–56. https://doi.org/10.1016/j.ijhydene.2022.05.250.
[37] Lee J, Park C, Kim Y, Choi Y, Bae J, Lim B. Effect of turbocharger on performance and thermal efficiency of hydrogen-fueled spark ignition engine. Int J Hydrogen Energy Feb. 2019;44(8):4350–60. https://doi.org/10.1016/j.ijhydene.2018.12.113.
[38] Barış O, Güler İ, Yaşgül A. The effect of different charging concepts on hydrogen fuelled internal combustion engines. Fuel Jul. 2023;343:127983. https://doi.org/10.1016/j.fuel.2023.127983.
[39] Wang K, et al. Performance optimization design of direct injection turbocharged hydrogen internal combustion engine. Appl. Energy Combust. Sci. Dec. 2023;16:100204. https://doi.org/10.1016/j.jaecs.2023.100204.
[40] Jilakara S, et al. An experimental study of turbocharged hydrogen fuelled internal combustion engine. SAE Int. J. Engines Jan. 2015;8(1):314–25. https://doi.org/10.4271/2015-26-0051.
[41] Güler İ, Kılıçaslan A, Küçük T, Corsini D. Transient and altitude performance analysis of hydrogen fuelled internal combustion engines with different charging concepts. Int J Hydrogen Energy Jan. 2024;49:1112–22. https://doi.org/10.1016/j.ijhydene.2023.10.104.
[42] Heintz N, Mews M, Stier G, Beaumont AJ, Noble AD. An approach to torque-based engine management systems. SAE International, Warrendale, PA, SAE Technical Paper 2001-01–0269 Mar. 2001. https://doi.org/10.4271/2001-01-0269.
[43] Hohmann S, Sackmann M, Krebs V. Nonlinear torque control of a spark ignition engine. IFAC Proc Jun. 2000;33(9):591–6. https://doi.org/10.1016/S1474-6670(17)38208-3.
[44] Livshiz M, Kao M, Will A. Validation and calibration process of powertrain model for engine torque control development. SAE International, Warrendale, PA, SAE Technical Paper 2004-01–0902 Mar. 2004. https://doi.org/10.4271/2004-01-0902.
[45] Castresana J, Gabiña G, Martin L, Basterretxea A, Uriondo Z. Marine diesel engine ANN modelling with multiple output for complete engine performance map. Fuel Jul. 2022;319:123873. https://doi.org/10.1016/j.fuel.2022.123873.
[46] Application of artificial neural network for internal combustion engines: a state of the art review | SpringerLink [Online]. Available: https://link.springer.com/article/10.1007/s11831-021-09596-5. [Accessed 27 September 2023].
[47] Zhou L, Song Y, Ji W, Wei H. Machine learning for combustion. Energy AI Jan. 2022;7:100128. https://doi.org/10.1016/j.egyai.2021.100128.
[48] Tosso HG, Jardim SAB, Bloise R, Santos MMD. Spark ignition engine modeling using optimized artificial neural network. Energies Sep. 2022;15(18):6587. https://doi.org/10.3390/en15186587.
[49] Ho T, Karri V, Lim D, Barret D. An investigation of engine performance parameters and artificial intelligent emission prediction of hydrogen powered car. Int J Hydrogen Energy Jul. 2008;33(14):3837–46. https://doi.org/10.1016/j.ijhydene.2008.04.037.
[50] Shahpouri S, Gordon D, Hayduk C, Rezaei R, Koch CR, Shahbakhti M. Hybrid emission and combustion modeling of hydrogen fueled engines. Int J Hydrogen Energy Jul. 2023;48(62):24037–53. https://doi.org/10.1016/j.ijhydene.2023.03.153.
[51] Javed S, Satyanarayana Murthy YVV, Baig RU, Prasada Rao D. Development of ANN model for prediction of performance and emission characteristics of hydrogen dual fueled diesel engine with Jatropha Methyl Ester biodiesel blends. J Nat Gas Sci Eng Sep. 2015;26:549–57. https://doi.org/10.1016/j.jngse.2015.06.041.
[52] Warey A, Gao J, Grover R. Prediction of engine-out emissions using deep convolutional neural networks. SAE Int J Adv Curr Pract Mobil Apr. 2021;3(6):2863–71. https://doi.org/10.4271/2021-01-0414.
[53] Millo F, et al. Synergetic application of zero-, one-, and three-dimensional computational fluid dynamics approaches for hydrogen-fuelled spark ignition engine simulation. SAE Int. J. Engines Dec. 2021;15(4):561–80. https://doi.org/10.4271/03-15-04-0030.
[54] Tuan Hoang A, et al. A review on application of artificial neural network (ANN) for performance and emission characteristics of diesel engine fueled with biodiesel-based fuels. Sustain Energy Technol Assessments Oct. 2021;47:101416. https://doi.org/10.1016/j.seta.2021.101416.
[55] Yang R, et al. An artificial neural network model to predict efficiency and emissions of a gasoline engine. Processes Jan. 2022;10(2):204. https://doi.org/10.3390/pr10020204.
[56] Veza I, et al. Review of artificial neural networks for gasoline, diesel and homogeneous charge compression ignition engine. Alex Eng J Nov. 2022;61(11):8363–91. https://doi.org/10.1016/j.aej.2022.01.072.
[57] Shethia FP, Mecagni J, Brusa A, Cavina N. Development and software-in-the-loop validation of an artificial neural network-based engine simulator. In: Presented at the conference on sustainable mobility; Sep. 2022. https://doi.org/10.4271/2022-24-0029. 2022-24–0029.
[58] Galushkin AI. Neural networks theory. Springer Science & Business Media; 2007.
[59] Chen SK, Flynn PF. Development of a single cylinder compression ignition Research engine. SAE International, Warrendale, PA, SAE Technical Paper Feb. 1965:650733. https://doi.org/10.4271/650733.
[60] Mavropoulos GC, Rakopoulos CD, Hountalas DT. Experimental investigation of instantaneous cyclic heat transfer in the combustion chamber and exhaust manifold of a DI diesel engine under transient operating conditions. In: Presented at the SAE world congress & exhibition; Apr. 2009. https://doi.org/10.4271/2009-01-1122. 2009-01–1122.
[61] Mezher H, Chalet D, Migaud J, Chesse P. Frequency based approach for simulating pressure waves at the inlet of internal combustion engines using a parameterized model. Appl Energy Jun. 2013;106:275–86. https://doi.org/10.1016/j.apenergy.2013.01.075.
[62] J. Heywood, Internal combustion engine fundamentals. McGraw-Hill..
[63] Chiong MS, Rajoo S, Martinez-Botas RF, Costall AW. Engine turbocharger performance prediction: one-dimensional modeling of a twin entry turbine. Energy Convers Manag May 2012;57:68–78. https://doi.org/10.1016/j.enconman.2011.12.001.
[64] Moraal P, Kolmanovsky I. Turbocharger modeling for automotive control applications. In: Presented at the international congress & exposition; Mar. 1999. https://doi.org/10.4271/1999-01-0908. 1999-01–0908.
[65] Nakhjiri M, Pelz P, Matyschok B, Däubler L, Horn A. Physical modeling of automotive turbocharger compressor: analytical approach and validation. In: Presented at the commercial vehicle engineering congress; Sep. 2011. https://doi.org/10.4271/2011-01-2214. 2011-01–2214.
[66] Chacartegui R, Sánchez D, Muñoz A, Sánchez T. Real time simulation of medium size gas turbines. Energy Convers Manag Jan. 2011;52(1):713–24. https://doi.org/10.1016/j.enconman.2010.07.050.
[67] Venson GG, Barros JEM. Turbocharger dynamic analysis using first order system step response. In: Volume 6: structures and dynamics, parts A and B. Orlando, Florida, USA: ASMEDC; Jan. 2009. p. 935–40. https://doi.org/10.1115/GT2009-59822.
[68] Azeem N, et al. Experimental study of cycle-by-cycle variations in a spark ignition internal combustion engine fueled with hydrogen. Int J Hydrogen Energy Mar. 2024;60:1224–38. https://doi.org/10.1016/j.ijhydene.2024.02.182.
[69] Li X, Sun B, Zhang D, Wang X, Bao L, Luo Q. Experimental study on the cycle variation characteristics of direct injection hydrogen engine. Energy Convers Manag X Aug. 2022;15:100260. https://doi.org/10.1016/j.ecmx.2022.100260.
[70] Sun B, Zhang D, Liu F. Cycle variations in a hydrogen internal combustion engine. Int J Hydrogen Energy Mar. 2013;38(9):3778–83. https://doi.org/10.1016/j.ijhydene.2012.12.126.
[71] Cavina N, Brusa A, Rojo N, Corti E. Statistical analysis of knock intensity probability distribution and development of 0-D predictive knock model for a SI TC engine. In: Presented at the WCX world congress experience; Apr. 2018. https://doi.org/10.4271/2018-01-0858. 2018-01–0858.
[72] Forte C, Corti E, Bianchi GM, Falfari S, Fantoni S. A RANS CFD 3D methodology for the evaluation of the effects of cycle by cycle variation on knock tendency of a high performance spark ignition engine. In: Presented at the SAE 2014 world congress & exhibition; Apr. 2014. https://doi.org/10.4271/2014-01-1223. 2014-01–1223.
[73] Scocozza GF, et al. Development and validation of a virtual sensor for estimating the maximum in-cylinder pressure of SI and GCI engines. In: Presented at the 15th international conference on engines & vehicles; Sep. 2021. https://doi.org/10.4271/2021-24-0026. 2021-24–0026.
[74] Cavina N, Businaro A, Cesare MD, Monti F, Cerofolini A. Application of acoustic and vibration-based knock detection techniques to a high speed engine. SAE International, Warrendale, PA, SAE Technical Paper 2017-01–0786 Mar. 2017. https://doi.org/10.4271/2017-01-0786.
[75] Millo F, Ferraro CV. Knock in S.I. Engines: a comparison between different techniques for detection and control. SAE Trans 1998;107:1091–112.
[76] Corti E, Abbondanza M, Ponti F, Raggini L. The use of piezoelectric washers for feedback combustion control. SAE Int J Adv Curr Pract Mobil Apr. 2020;2(4). https://doi.org/10.4271/2020-01-1146. Art. no. 2020-01–1146.

[77] Naber JD, Szwaja S. Statistical approach to characterize combustion knock in the hydrogen fuelled SI engine. J KONES 2007;14(3):443–50.
[78] Cavina N, Rojo N, Businaro A, Cevolani R. Comparison between pressure- and ion-current-based closed-loop combustion control performance. SAE Int. J. Engines Apr. 2019;12(2). https://doi.org/10.4271/03-12-02-0016. 03-12-02–0016.
[79] Corti E, et al. Transient spark advance calibration approach. Energy Proc 2014;45: 967–76. https://doi.org/10.1016/j.egypro.2014.01.102.
[80] Rao A, Liu Y, Ma F. Study of NOx emission for hydrogen enriched compressed natural along with exhaust gas recirculation in spark ignition engine by Zeldovich' mechanism, support vector machine and regression correlation. Fuel Jun. 2022; 318:123577. https://doi.org/10.1016/j.fuel.2022.123577.
[81] A super-extended zel'dovich mechanism for No x modeling and engine calibration on JSTOR [Online]. Available: https://www.jstor.org/stable/44736596. [Accessed 29 September 2023].
[82] Glarborg P. Detailed kinetic mechanisms of pollutant formation in combustion processes. In: Computer aided chemical engineering. vol. 45. Elsevier; 2019. p. 603–45. https://doi.org/10.1016/B978-0-444-64087-1.00011-5.
[83] Williams A. Pollutant formation and control. In: Combustion of liquid fuel sprays. Elsevier; 1990. p. 127–60. https://doi.org/10.1016/B978-0-408-04113-3.50009-9.